Key Points:
- Magnetic measurements and microscopic observation indicate exsolved titanohematite is the main source of natural remanent magnetization
- Data inversions confirm magnetic enhancement from microstructure in titanohematite and weak contribution of multidomain hematite to the NRM
- Inversion results are consistent with bulk measurements and indicate little effect of alternating field demagnetization on the NRM

Supporting Information:
- Supporting Information S1

Correspondence to:
Z. Pastore,
zeudiap@hotmail.com; zeudia.
pastore@ntnu.no

Mapping and Modeling Sources of Natural Remanent Magnetization in the Microcline–Sillimanite Gneiss, Northwest Adirondack Mountains: Implications for Crustal Magnetism

Z. Pastore[1] , **S. A. McEnroe[1]** , **N. S. Church[1]** , and **H. Oda[2]**

[1]Department of Geoscience and Petroleum, Norwegian University of Science and Technology, Trondheim, Norway, [2]Geological Survey of Japan, National Institute of Advanced Industrial Science and Technology (AIST), Tsukuba, Japan

Abstract Distinct crustal remanent magnetic anomalies are a strong indicator of rocks with stable natural remanent magnetization (NRM) carriers. The latter are able to store information on the history of a rock over long geological periods, and can therefore be used for a variety of applications in the field of paleomagnetism and rock magnetism. Typically, paleomagnetic and rock-magnetic studies rely on rocks bulk magnetic properties. With the advent of high-resolution magnetometric scanning techniques, it is now possible to map magnetic sources at the mineral scale, identify the different magnetic carriers, and analyze the effect of geometry, microstructures, and composition on their magnetic response. We investigate the stability of discrete remanent magnetization sources of a microcline–sillimanite gneiss sample from Russell Belt with a strong NRM, by scanning the sample before, and after alternating field demagnetization to 100 mT. We quantified changes in the magnetization intensity and direction by inverting the magnetic scan data. Here, we confirm that the exsolved titanohematite with ilmenite lamellae is the major source of magnetization, and the coexisting multidomain hematite grains contribute little to the NRM, or the magnetic anomalies. The microstructures in the titanohematite control local magnetic properties at the mineral scale. Magnetic modeling results suggest a consistent average magnetization direction before and after demagnetization at both the grain and thin section scale, with a decrease in the magnetization intensity of ≈30%. Results are consistent with previous bulk magnetic measurements and the likelihood to use high-resolution magnetometric techniques in future magnetic studies is high.

Plain Language Summary The magnetism recorded in rocks is a useful tool to study our planet's history and can be a blueprint for the design of modern information storage systems. The stability of the magnetic record is a main issue for many applications, and microstructure in minerals can play a major role. In early studies, the influence of microstructure on the magnetic properties of individual grains was an elusive topic; now, it is possible to investigate this link through high-resolution imaging techniques, advanced micromagnetic simulations, and laboratory techniques. We used a modern magnetic technique that maps the magnetic response over a thin rock slice with submillimeter spatial resolution. We used these data to identify grains yielding different magnetic responses from a sample that has bulk magnetic properties, which indicate a stable magnetic record. To investigate the magnetic stability of individual grains, we acquired data before and after partial removal of the magnetization of the sample and estimated the changes in the magnetic properties at both the grain and sample scale by modeling the magnetic response. Results are consistent with the bulk magnetic properties and indicate that the sample efficiently held the magnetization and that grains' microstructure has a strong effect on local magnetic properties.

1. Introduction

Rock-magnetic properties vary depending on amount, composition, microstructure, and size of magnetic grains. This variability affects the capability of the rocks to retain a stable magnetic memory, a property central to the fields of paleomagnetism, environmental magnetism, rock magnetism, and exploration. Modern scanning magnetometric techniques map magnetic anomalies caused by individual minerals within rocks with submillimeter resolution. These data can be used to quantify individual magnetizations and to identify

the stability of the natural remanent magnetization (NRM) of an individual grain or an assemblage of grains in a rock. This information is critical to the study of the past history of the Earth's magnetic field and is also a key tool to interpret magnetic anomalies on Earth and other rocky planetary bodies. The mineral sources and nature of remanent magnetization reflected in crustal magnetic anomalies are ongoing topics of research (Brown & McEnroe, 2008; Clark, 1999; Ferré et al., 2021; McEnroe et al., 2002, 2018; McEnroe, Brown, et al., 2009; McEnroe, Fabian, et al., 2009; McEnroe, Robinson, et al., 2001; Michels et al., 2018, 2020; Purucker & Whaler, 2007; ter Maat et al., 2019, 2020).

Here, we investigate a sillimanite microcline gneiss (GMS) sample from the Russell Belt (RB) in the northwest Adirondack Mountains, New York, which forms part of the southernmost exposure of the Grenville Province of North America. The GMS rocks are interpreted to have been felsic volcanic rocks hydrothermally altered in their primary environment, then metamorphosed to granulite grade (McEnroe & Brown, 2000) with peak metamorphic temperatures up to 800°C and pressures up to 8 kbar at ~1,050 Ma (Bickford et al., 2008; Bohlen et al., 1985; Spear & Markussen, 1997). These conditions would have completely reset preexisting magnetic directions. The rocks of the GMS unit commonly contain microcline, sillimanite, and locally garnet. Although some GMSs are rich in magnetite, other areas of the GMS, such as the RB, are virtually magnetite free and titanohematite with exsolution lamellae of ilmenite and rutile is the dominant iron oxide (Balsley & Buddington, 1957, 1958; Buddington & Leonard, 1962). The RB rocks were originally described by Balsley and Buddington (1957) and later studied by McEnroe and Brown (2000) for their rock-magnetic properties and the strong association of reversed NRM directions with a large negative (below background) aeromagnetic anomaly.

Balsley and Buddington (1954) were first to recognize the unusual nature of the negative anomalies of the RB, which were recorded in one of the first aeromagnetic surveys flown. The aeromagnetic data were acquired by the US Geological Survey (USGS) in 1945 at an altitude of 304.8 m and with a flight line spacing of 0.4 km. McEnroe and Brown (2000) later collected ground-magnetic data along two profiles in the RB area, associated with a distinct negative aeromagnetic anomaly of ≈3,500 nT below background (Figure 1). Brown and McEnroe (2012) report data on the 14 GMS paleomagnetic sites including six from the RB. The RB sites have an average NRM with a mean vector intensity (Int) of 3.5 A/m, steep negative inclination (Inc) of −59°, declination (Dec) of 258°, and an average susceptibility of 2.3×10^{-3} (SI) (McEnroe & Brown, 2000). We selected a sample from site AD34 (Figure 1) which has a site average susceptibility of 2×10^{-3} (SI), NRM Int of 7.6 A/m, steep negative inclination of −53°, and declination of 262°. The Königsberger ratio (Q value) is 358 (McEnroe & Brown, 2000), calculated as the ratio between the NRM and the induced magnetization (susceptibility × local magnetic field).

Using scanning magnetic microscopy (SMM), we further investigated the sources of this large and stable NRM, and the local effect of mineral microstructures on the magnetization. SMM is well suited to this aim because it allows for mapping of magnetic anomalies created by variations of magnetization at the mineral scale (Church & McEnroe, 2018; Egli & Heller, 2000; Hankard et al., 2009; Lima & Weiss, 2016; Oda et al., 2011; Pastore et al., 2018, 2019; Weiss et al., 2002). The focus of this paper is sample AD34-6b which has a susceptibility value of 3×10^4 (SI), NRM of 8.2 A/m, and a Q value of 598 (McEnroe & Brown, 2000). The magnetic response of this sample is completely dominated by remanence. Modeling of the mineral magnetic anomalies was used to quantify the small-scale variation of the magnetization between and within grains and to verify the link between microstructure and magnetization. In addition, comparison of bulk properties with the calculated magnetization of constituent mineral grains allows us to assess if SMM techniques can accurately attribute total response to the summed contribution of individual particles or phases.

2. Materials and Methods

2.1. Petrography and Mineral Chemistry

The GMS unit of the RB has an oxide mineralogy dominated by the Fe_2O_3–$FeTiO_3$ system, described in detail by McEnroe and Brown (2000). Sample AD34-6b was chosen for a magnetic scan because of the extensive petrographic and petrological information from site AD34. Samples from site AD34 contain millimeter-to-micron sized titanohematite grains with abundant exsolution lamellae of ilmenite ($FeTiO_3$) and
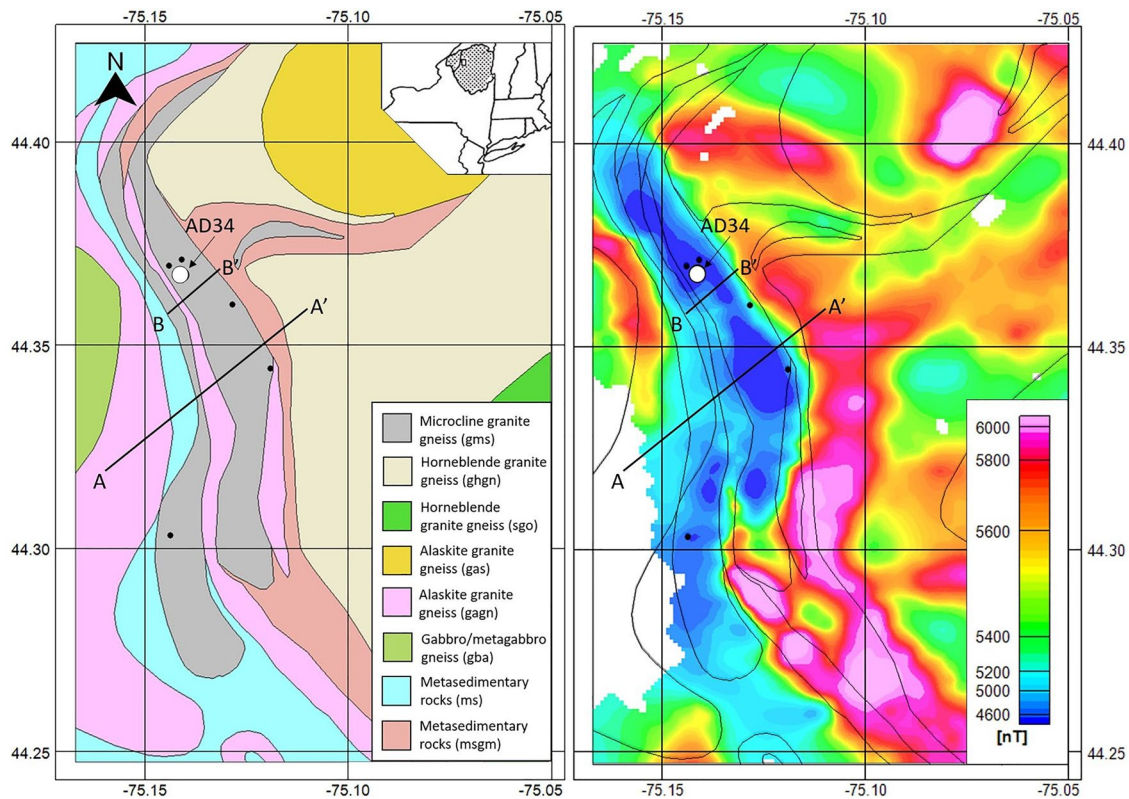
Figure 1. Geological and aeromagnetic maps (modified from Balsley and Buddington [1958]) of part of the Russell Belt. Total magnetic intensity data are relative to arbitrary datum in Balsley and Buddington (1958). Compiled data are available at the USGS data airborne geophysical surveys catalog (https://mrdata.usgs.gov/magnetic/show-survey.php?id=NY0107_pg.shp). Sampling site locations from McEnroe and Brown (2000) are shown in both maps with black circles, and the study sample site AD34 is shown with a white circle. A–A′ and B–B′ mark ground-magnetic profiles from McEnroe and Brown (2000). The magnetic anomaly in the ground-magnetic survey along profile B–B′, near to site AD34, reaches a local minimum value of −4,800 nT relative to a field intensity of 58,000 nT. Latitudes and longitudes are given in the World Geodetic coordinate system (WGS84). USGS, US Geological Survey.

minor pyrophanite ($MnTiO_3$) lamellae parallel to (0001) plane of the titanohematite. Rutile, spinel, and corundum exsolution features are also common. Multiple generations of exsolution lamellae range from the micron scale down to the nm scale (Kasama et al., 2004). Titanohematite is the dominant oxide, and magnetite is either absent or very rare. In addition, some samples contain large multidomain (MD) near end-member hematite grains with no or minor ilmenite exsolution and abundant rutile needles. Electron microprobe (EMP) analyses indicated that the titanohematite compositions are in the range of hem_{85-81} and ilmenite lamellae from ilm_{98-91}. Energy-dispersive X-ray spectroscopy of the transmission electron microscopy samples AD34-4 and AD34-5 with a smaller beam size reduced the composition range to hem_{92-88}, showing that the EMP data included overlap analyses of nm-scale lamellae (Kasama et al., 2004). The lamellae of ilmenite ($FeTiO_3$) and pyrophanite ($MnTiO_3$) range from the micron size to <2 nm. Both McEnroe and Brown (2000) and Kasama et al. (2004) suggest that the strong NRM is linked to the amount of fine exsolution lamellae in the titanohematite. McCammon et al. (2009) used Mössbauer spectroscopy to study the relation between nanoscale lamellae and host material on sample AD34-1. They confirmed the presence of Ti in solid solution by the deviation of the hyperspectral field and determined a composition for the host titanohematite of $tihem_{92-91}$ and ilm_{100-95}. Mössbauer data confirm that there is up to 8% Ti remaining in solid solution in the titanohematite. Previously, interfaces of exsolution lamellae of ilmenite in hematite have been identified as the source of intense remanent magnetism in oxide intergrowths of phases normally considered to be only weakly magnetic (Kasama et al., 2009; McEnroe et al., 2002, 2007, 2016; McEnroe, Brown, et al., 2009; McEnroe, Harrison et al., 2001; Robinson et al., 2002, 2004, 2016; Robinson, Harrison, et al., 2006). Here, we are able to verify this concept at the mineral scale.
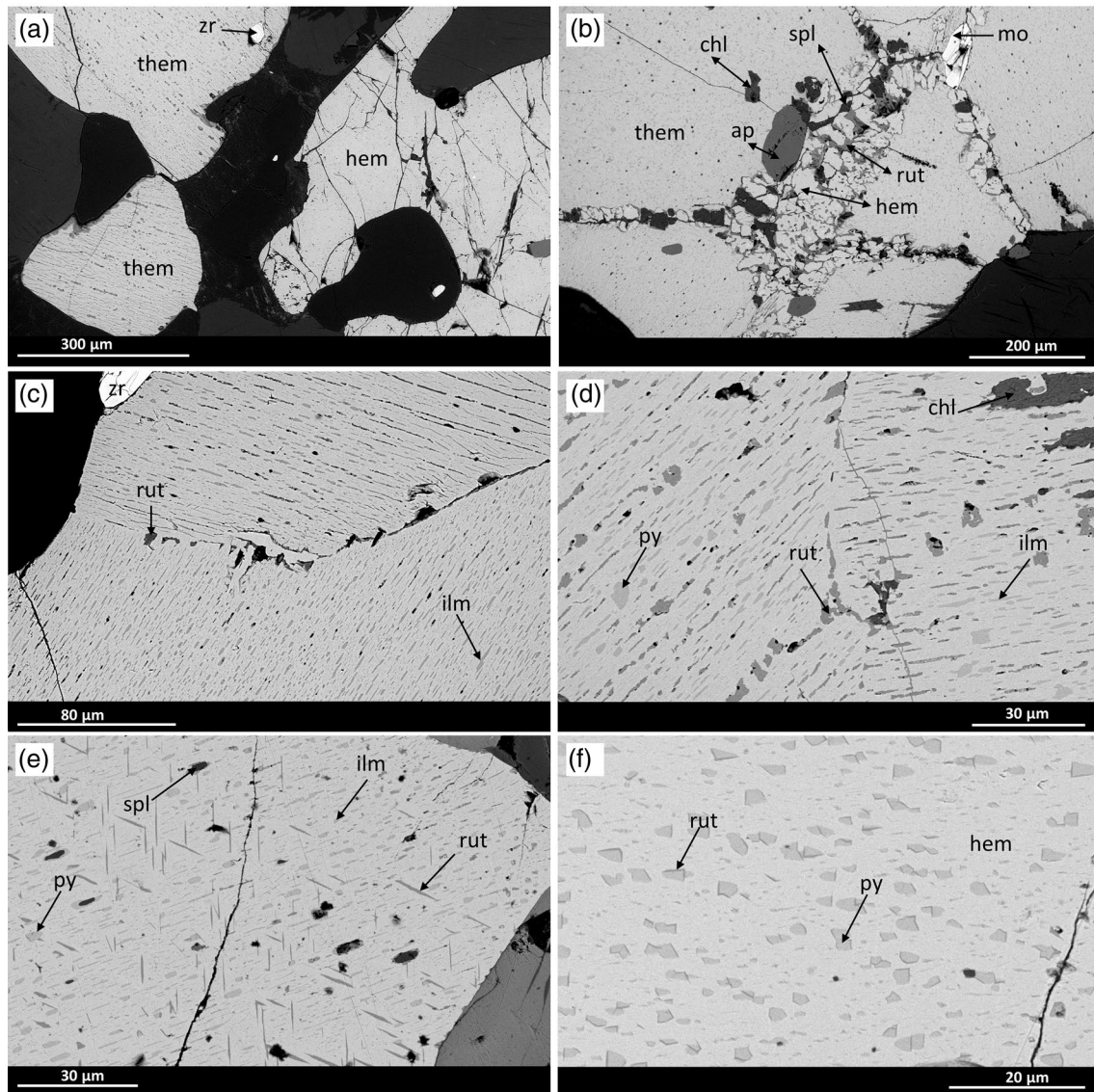
Figure 2. Backscattered electron images of sample AD34-6b. (a) Exsolved titanohematite (them) and hematite (hem) grains. (b) Titanohematite host with symplectite of hematite, rutile (rut), and spinel (spl) in the middle. Apatite (ap) and chlorite (chl) appear in dark gray colors. On the upper-right side of the image is a bright monazite grain. (c) Titanohematite with exsolution lamellae of ilmenite (ilm) oriented in different directions. Rutile is darker gray and has a larger size at grains boundaries. (d) Titanohematite with exsolution lamellae of ilmenite and pyrophanite (py). Rutile appears in darker gray. In the upper-right corner, chlorite is a dark gray color. (e) Titanohematite with fine ilmenite lamellae and larger pyrophanite blebs. Rutile needles and spinel in darker gray. (f) Pyrophanite blebs in hematite host with fine plate-like rutile lamellae.

To identify the phases and map the distribution of the opaque minerals in the thin section, we used optical microscopes and a Phenom XL scanning electron microscope (SEM) at the NTNU Rock and Paleomagnetism laboratory. A backscattered electron (BSE) map was made of the entire thin section, in addition to higher resolution SEM images of individual oxide grains. The BSE map is used to correlate the mapped magnetic anomalies with the oxides. Figure 2 shows the variation of oxides in AD34-6b. The BSE images are consistent with what was observed in earlier studies. Titanohematite with abundant exsolution lamellae is the dominant oxide. At grain boundaries of some composite grains, a symplectite of hematite–rutile and ±spinel is present, likely a product of the breakdown of pseudobrookite (Fe_2TiO_5) during cooling from granulite metamorphic conditions (McEnroe & Brown, 2000). Large end-member hematite grains contain rutile needles, and minor chlorite is present in some hematite and titanohematite grains. Monazite, zircon, and apatite are common inclusions in the oxides.

2.2. Rock-Magnetic Properties

Major and minor hysteresis loops are powerful tools to identify magnetic phases and inform predictions about domain state, remagnetization processes, and remanence stability. To characterize the magnetic carriers of sample AD34-6b, hysteresis measurements were acquired using a Princeton Measurement Corp. MicroMag 3902 vibrating sample magnetometer. Major hysteresis loops were acquired with maximum fields of 1.1 T and a linear fit to the data above 1 T was applied to correct for the paramagnetic component. To minimize the influence of the strong magnetocrystalline anisotropy of hematite, which constrains magnetization to the basal plane, hysteresis loops were acquired in 10° steps for a full rotation of the specimen. For each orientation, the shape parameter, σ_{hys} (Fabian, 2003), was calculated to identify those in which mineral fabric strongly influences magnetic properties. The orientation in which σ_{hys} is closest to 0 minimizes coercivity enhancement by subpopulations of grains with an unfavorable alignment to the applied field and best measures average intrinsic properties. This orientation was used for subsequent measurements.

First-order reversal curves (FORCs; Roberts et al., 2014, and references therein) and nonlinear Preisach maps are sensitive techniques to identify secondary phases and examine the switching behavior and domain states of magnetic carriers. FORCs were acquired with a saturating field of 1.1 T and with a field increment of 5 mT. The FORC distribution was calculated using FORCinel (Harrison & Feinberg, 2008) with VARIFORC (Egli, 2013) smoothing parameters $S_{b,0} = 7$, $S_{b,1} = S_{c,0} = S_{c,1} = 5$, $\lambda = 0.07$. Nonlinear Preisach maps (Church et al., 2016) measure remanence magnitude, rather than magnetization density as in FORCs, acquired and calculated in approximately logarithmic steps. The Preisach map presented here was calculated from 91 nonlinear remanence curves using a saturating field of 1.1 T.

The major hysteresis loop confirms that the AD34-6b sample is dominated by a high-coercivity carrier with strong magnetocrystalline anisotropy. The major hysteresis loop of the AD34-6b rock chip loop is visually closed only at the maximum field (Figure 3(a), inset) and the *F* test criterion proposed by Paterson et al. (2018) indicates that the data above 1 T are not linear. Therefore, while the bulk coercivity is 165 mT, there remains a component of magnetization with coercivity >1.1 T, the maximum field permitted by the instrument geometry. The ratio of saturation remanence to saturation magnetization (M_{rs}/M_s) is 0.66. Although the inability to saturate the sample introduces imprecision, this value is well above the theoretical maximum of 0.5 for shape anisotropy-dominated single-domain particles (Stoner & Wohlfarth, 1948).

The saturation magnetization of whole rock chip is 23 mA m^2/kg. Image processing of the BSE scan described above yields an oxide content of 4%, indicating that the M_s of the oxide phases alone is 0.58 A m^2/kg or 3,000 A/m. Such values are 40%–100% larger than literature values for single-phase hematite (e.g., Özdemir & Dunlop, 2014) and quantify the magnetic enhancement from the interface moments of the exsolved titanohematite (Robinson et al., 2002, 2004). The M_{rs} of the oxides alone is 2,000 A/m, which serves as an absolute upper limit for magnetization values obtained from inversion of scanning data.

FORC analysis (Figure 3(b)) allows finer examination of the microcoercivity distribution and can reveal potential secondary phases. The presence of trace amounts of magnetite can be inferred from the extremely weak positive signal near the origin that extends along the B_c axis to 30 mT. Due to the resolution of the measurement, it is challenging to interpret the domain state of this phase, but the weak intensity and limited spatial extent of its FORC distribution indicates that it contributes very little to the total response. The dominant signal in the FORC diagram is a positive peak centered at 150 mT, elongated parallel to the B_c axis and offset to negative B_u values, which broadens and shifts to larger negative B_u values at higher B_c. A negative peak is also present below the positive peak and similarly extends to still larger negative B_u values with higher B_c. These features are typical of hematite FORC diagrams, including those with interface moments (e.g., Brownlee et al., 2011; Muxworthy et al., 2005). Harrison et al. (2019) simulated assemblages of particles with hexagonal magnetocrystalline anisotropy such as observed in hematite, and argued that the presence of multiple easy axes within the basal plane produces the positive and negative signals observed in hematite FORC diagrams. However, very similar FORC distributions were measured and simulated by Schrefl et al. (2012) in Nd$_2$Fe$_{14}$B, a material that exhibits strong *uniaxial* anisotropy, but that also develops a "core–shell" structure at grain boundaries that behaves as an exchange spring. Both hexagonal magnetocrystalline anisotropy and exchange coupling between the host and interface layers are predicted in exsolved titanohematite, so the observed FORC diagram may be a combination of the two processes.
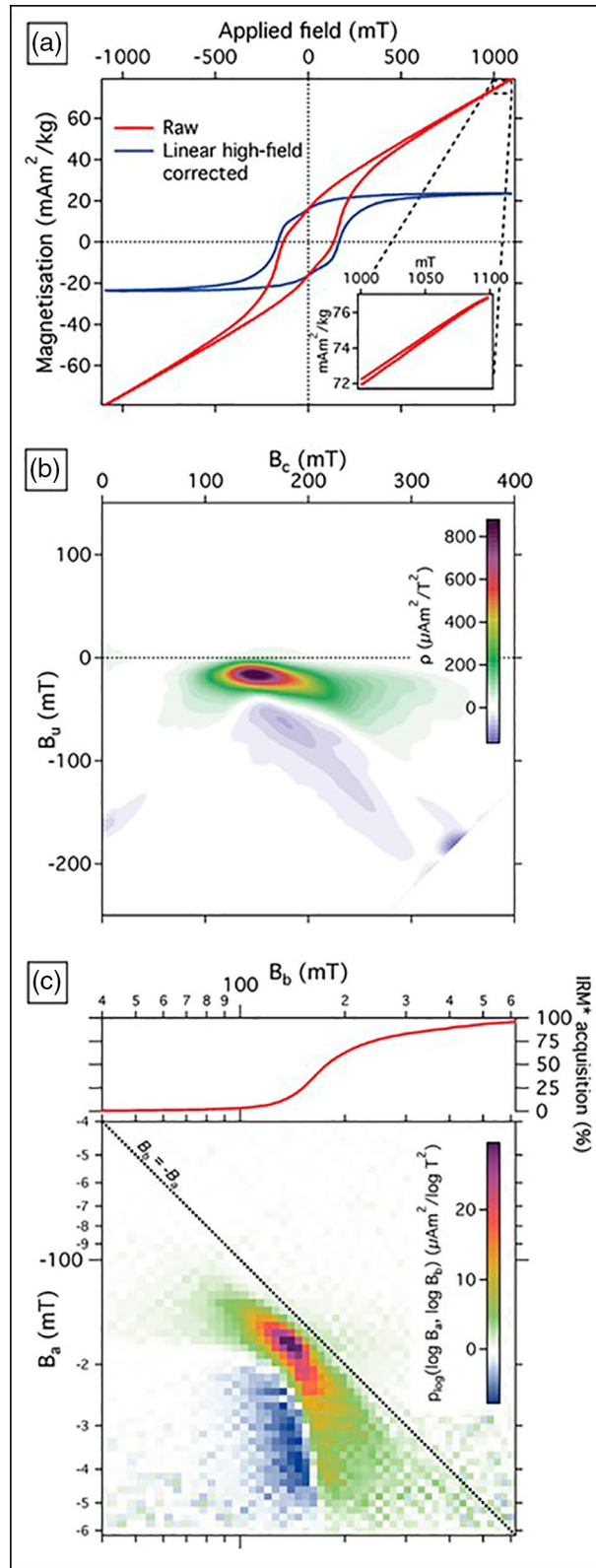
Figure 3. Rock-magnetic characterization of AD34-6b. (a) Major hysteresis loop, with loop corrected for high-field slope using linear fit above 1 T, (b) FORC diagram showing offset positive and negative peaks characteristic of hematite and signal near origin deriving from trace amounts of magnetite, and (c) Nonlinear Preisach map showing remanence behavior for fields 40 < (|Ba|, Bb) < 600 mT. FORC, first-order reversal curve.

Nonlinear Preisach maps avoid the need for smoothing by measuring purely remanence response and by acquiring and calculating the distribution using logarithmic field steps, and therefore serve as verification of the features observed in the FORC diagram. The signals in the Preisach map (Figure 3(c)) and FORC diagram are similar for the region of Preisach space that they share: a positive peak centered at $B_a = -170$, $B_b = 140$ mT, offset below $B_b = -B_a$ diagonal, and negative peak associated with it and further offset from the diagonal. The intensity of the highest-field data points ($|B_a| > 200$, $B_b > 150$ mT) of the positive peak is slightly enhanced in the Preisach map. This enhancement may be an effect of the logarithmic spacing of the measurement fields but may also reflect viscous processes that differ between the FORC and remanence measurements. The calculated isothermal remanent magnetization acquisition curve (Church et al., 2016) shows that only 3% of the 1.1 T saturation remanence is held by carriers with coercivity <100 mT, and nearly 20% is held by grains with coercivity >300 mT (Figure 3(c)).

2.3. Scanning Magnetic Microscopy

Magnetic scans of a 30-μm-thick thin section were made with a SQUID microscope at the Geological Survey of Japan (GSJ), National Institute of Advanced Industrial Science and Technology (AIST). The instrument measures the vertical component (Bz) of the field and imaging is carried out at room temperature (~25°C) in near-field-free conditions to characterize the magnetic remanence field. The nominal sampling step for all scans is 100 μm in *x* and *y* directions. The SQUID microscope system uses a 200 × 200 μm square washer type pickup coil, which has a field noise of 1.1 pT/√Hz at 1 Hz (Kawai et al., 2016), and a sample stage with positioning accuracy of ~10 μm (Oda et al., 2016).

Two magnetic scans were made before (NRM) and after alternating field (AF) demagnetization to 100 mT with tumbling in two axes, hereafter referred to as "AF demagnetization," with a sensor-to-sample distance of 252 and 255 μm, respectively. The sensor-to-sample distance was estimated by averaging three line current scans with a precision current source prior to each measurement using a software *SQUID LineScan* (Oda et al., 2016). The measured Bz ranges between −11,912 and 11,196 nT in the NRM scan (Figure 4) and from −6,090 to 6,119 nT in the AF scan. The least significant bit of the AD converter for the measured range was ~3.2 nT and measurements started from zero at a position more than 2 cm away from the thin section. Because of the low drift of flux-locked loop (Kawai et al., 2016) and the high-performance magnetic shielding (Oda et al., 2016), both measurements did not have any detectable drift nor any spike noises from the start to the end. A manual alignment was applied to register the magnetic scans with a higher resolution BSE image of the thin section. The overlay of these images shows a correlation between the mapped magnetic anomalies and the oxides (Figure 4). Most opaque grains are titanohematite with abundant exsolution lamellae. The few opaque grains showing weak magnetic anomalies are hematite with rare or no exsolution (area 3, Figure 4(a)). The opaques result in discrete, mostly isolated magnetic anomalies of varying amplitude, wavelength, and shape. Closely spaced opaque grains, or larger grains, are commonly associated with more complex anomalies as shown in the enlarged views in Figure 4 (areas 3, 4, 6, and S4).

To characterize the fine-scale remanent magnetization of the magnetic minerals, we applied inverse modeling of the magnetic scans data using Tensor Research ModelVision software (Oldenburg & Pratt, 2007; Pratt et al., 2006). The software allows 3-D modeling of the sources of magnetic anomalies and solves the nonlinear inverse problem using the Levenberg–Marquardt algorithm (Levenberg, 1944; Marquardt, 1963), where the intensity, declination, and inclination vary independently. The inversion procedure is iterative and runs along multiple parallel profiles until the standardized residual error between the input/measured data, and the calculated/modeled data are minimized along all profiles. Magnetic data were modeled using the geomagnetic coordinate system convention with the *x*–*y* plane parallel to the sample surface and *z* (vertical intensity) positive downward.

A key-constraint to improve the reliability of SMM inversions is the knowledge of the source geometry provided by optical and SEM microscopy. Discrete grains were modeled as uniformly magnetized prismatic bodies. Magnetic inversions were run on the entire thin section and on selected areas (Figure 4). For inversions on the entire thin section, grains were modeled as frustum bodies, that is, bodies with horizontal top and bottom bounded by polygons, which fill the volume occupied by the exsolved titanohematite or hematite grains (Figure 5). For inversions on selected areas, magnetic grains were additionally modeled by means of multiple adjacent tabular bodies filling the volume of the grain (Figures 6–9). Tabular bodies with areas
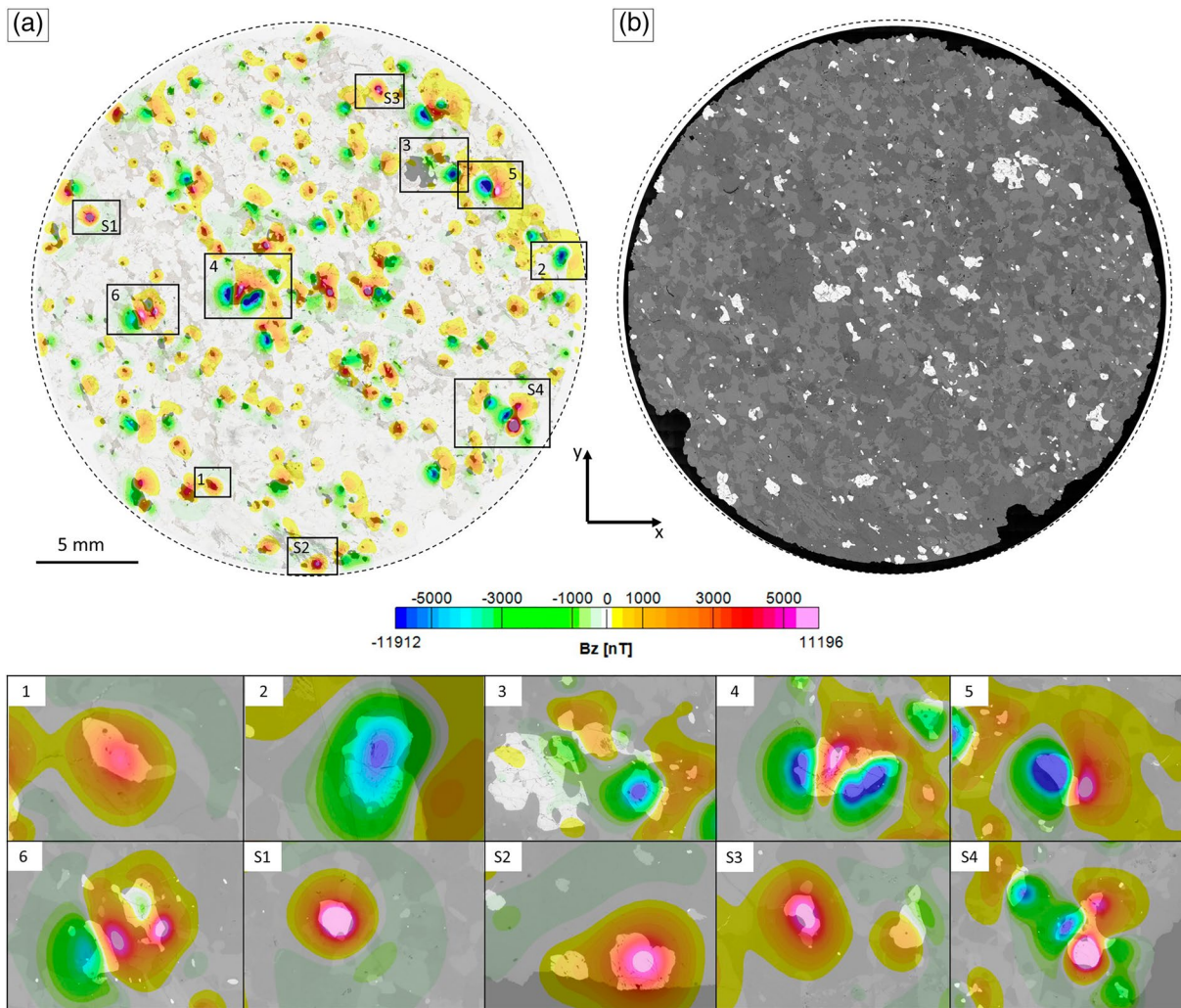
Figure 4. (a) Overlay of the NRM magnetic scan and optical photograph of the thin section; note that magnetic anomalies correlate well with the opaque mineralogy. (b) Backscattered electron (BSE) image with oxide mineralogy in bright contrast. Below, enlarged views of selected modeling areas showing the overlay of the measured magnetic data and the BSE image of the grains. NRM, natural remanent magnetization.

of 50 μm × 50 μm were used to resolve areas of change in magnetization direction and/or intensity within the grain, while simultaneously preserving the grain geometry. The sampling step of 100 μm in x and y directions of original measurements imposes a limitation on the spatial resolution of internal magnetization of the grains. According to the sampling theorem (Blakely, 1996; Nyquist, 1928; Shannon, 1948), we cannot obtain information at wavelengths smaller than a threshold of twice the sample interval (100 μm) which implies that we can resolve such variations over areas of approximately 200 μm × 200 μm. However, the use of tabular bodies with such areas does not allow for a good approximation of the grain geometry, which is a fundamental constraint in the inversions. Therefore, smaller tabular bodies were used to fill the volume of the grain and to define the model geometry. Both frustum and tabular bodies thicknesses were set to 30 μm. Ten areas were inverted using both frustum and tabular bodies, and six are shown in Figures 6–9, 12, and 13, with the remaining included in the Supplemental material (modeled areas S1–S4 in Figure 4).

Before running the inversion on the measured Bz data, the modeled bodies were assigned an initial magnetization value that approaches zero (~10^{-4} A/m), while magnetization inclination and declination angles were both set to zero. The ModelVision inversion package allows the imposition of upper and lower bounds for intensity and direction in the inversion process. Because most of the magnetic anomalies are isolated (discrete opaque grains surrounded by silicates), to model frustum bodies, we selected a large tolerance (the range by which each parameter can vary from its current value) of 10,000 A/m for the intensity of
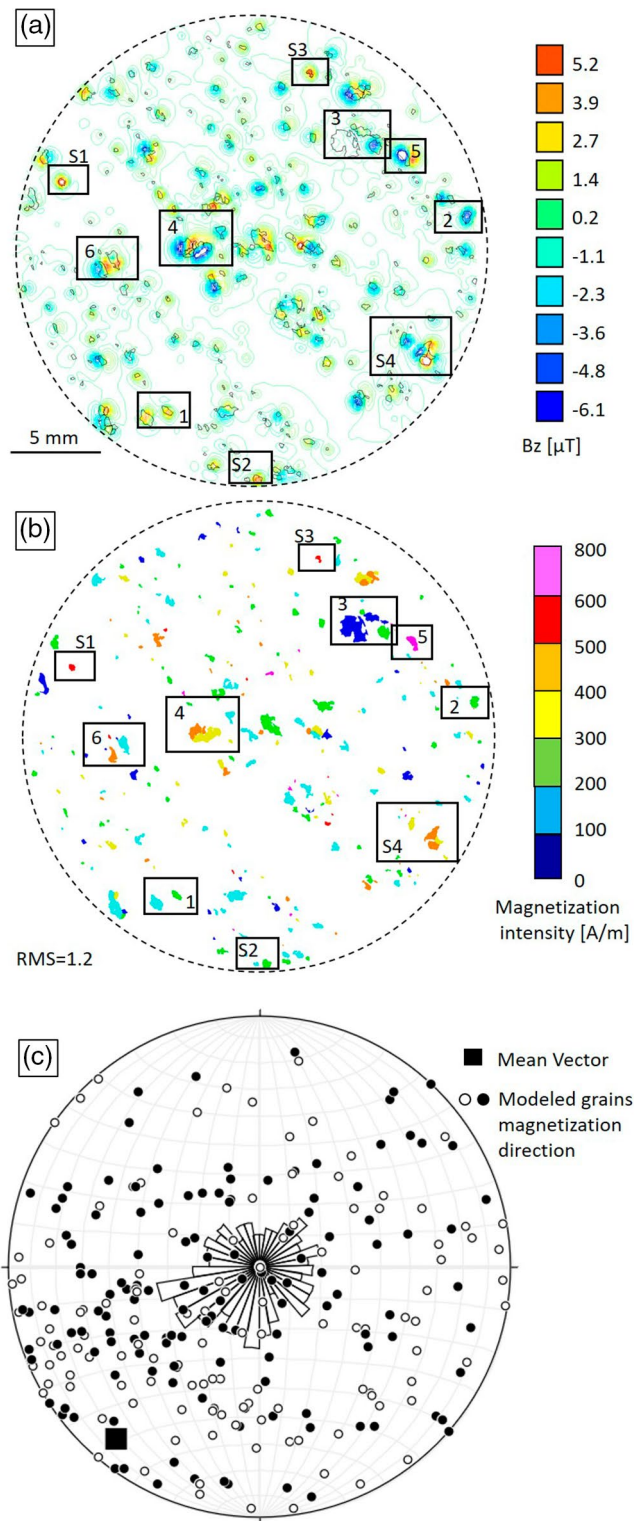
Figure 5. Data and inversion results prior to AF demagnetization. (a) Black boxes outline the area of the modeled grains. Overlaid are the contour lines of the magnetic data. (b) Bz full-scan inversion results with frustrum bodies color coded by magnetization intensity in A/m. (c) Stereoplot of magnetization direction for each modeled body with 10° bin rose diagram in the middle. Closed circles are for positive inclinations and the square indicates the standard mean vector direction, 12° inclination and 219° declination, calculated from all modeled grains by adding up the direction cosines of all of the individual unit vectors. AF, alternating field.
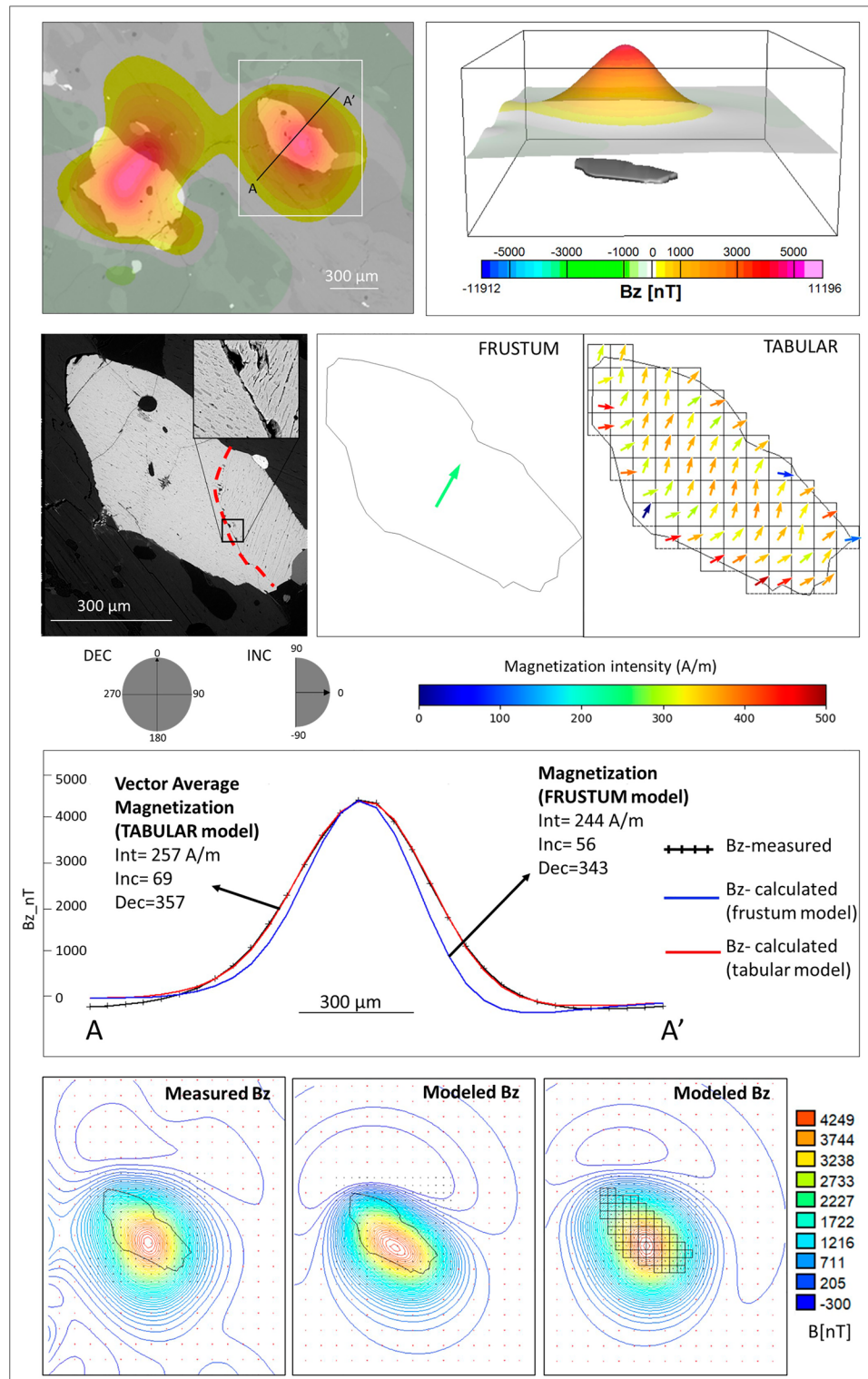
Figure 6. Top panel: map and 3D views of the magnetic anomaly measured over the grain (area 1, Figure 3). Upper middle panel: SEM image with enlarged view on internal grain boundary (dashed red line), and frustum and tabular-body models of the grain with arrows color coded by magnetization intensity and oriented according to inclination angle. The bright grain on the right side of the titanohematite is a monazite, dark circular grain within the titanohematite is a silicate phase. Middle panel: comparison of measured and calculated Bz for frustum, and tabular models along profile A–A′. Bottom panel: contour lines of calculated and measured Bz for both frustum and tabular bodies. Station points where Bz is calculated are shown in red dots. SEM, scanning electron microscope.

Figure 7. Top panel: map and 3D views of the magnetic anomaly measured over the grain (area 2, Figure 4). Upper middle panel: SEM image and frustum and tabular-body models of the grain with arrows color coded by magnetization intensity and oriented according to inclination angle. Middle panel: comparison of measured and calculated Bz for frustum and tabular models along profile AA′. Bottom panel: contour lines of calculated and measured Bz for both frustum and tabular bodies. Station points where Bz is calculated are shown in red dots. SEM, scanning electron microscope.
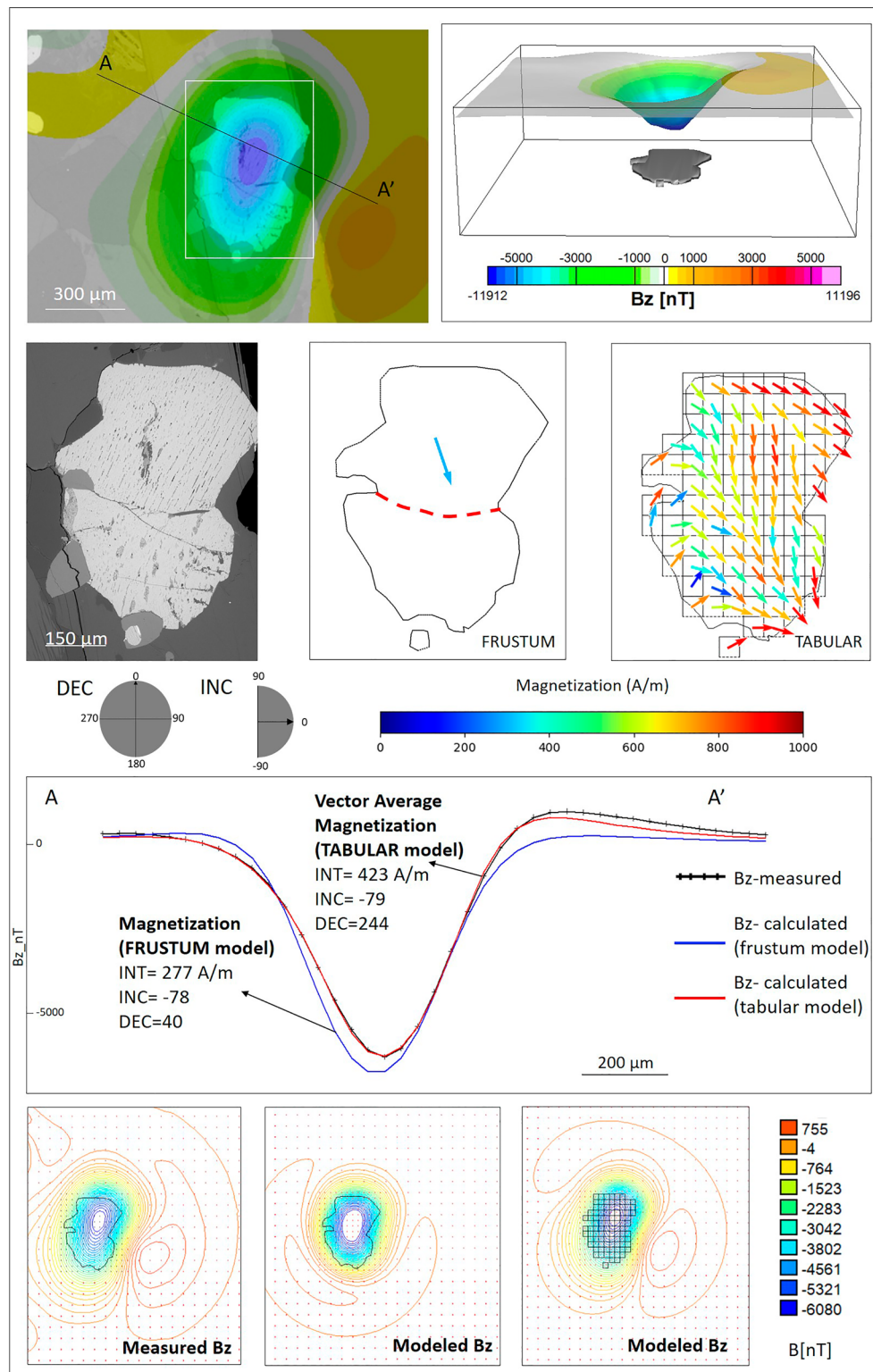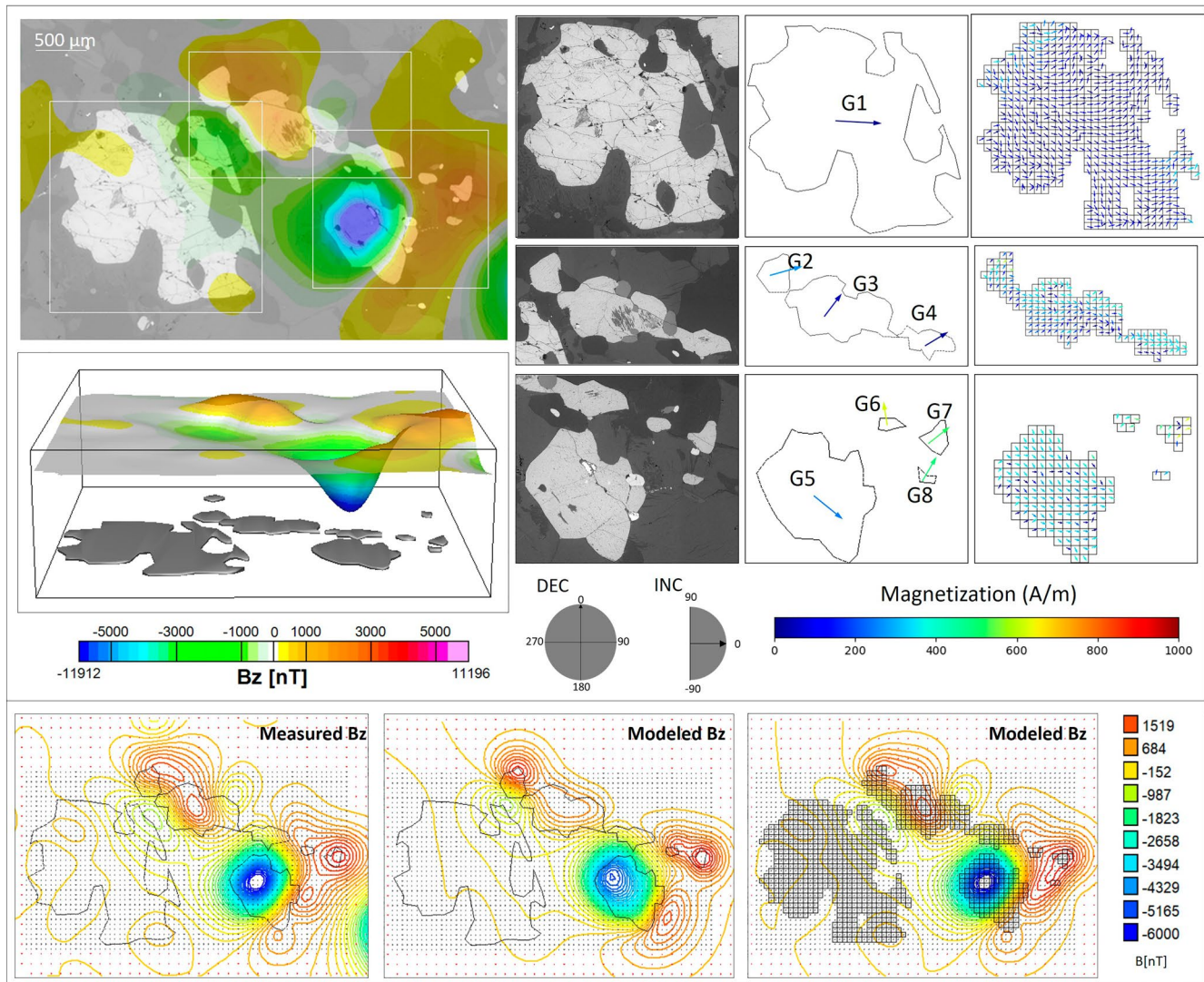
Figure 8. Left panel: map and 3D views of the magnetic anomaly measured over the grains from area 3 in Figure 4. Right panel: SEM images, frustum, and tabular-body models of the grains (G1, G2–G4, and G5–G8) with arrows color coded by magnetization intensity and oriented according to inclination angle. G1 is a large hematite, while G2–G8 are titanohematite grains with ilmenite lamellae, and exsolution of rutile and spinel. Small bright grains are monzonite. Bottom panel: contour lines of calculated and measured Bz for both frustum and tabular bodies. Station points where Bz is calculated are shown in red dots. SEM, scanning electron microscope.

the magnetization, while leaving the magnetization direction completely free. For the selected subregions, when each mineral source was discretized by multiple tabular bodies the inversion was run in multiple steps, using a set tolerance for the magnetization intensity at each step, and free magnetization direction. Pastore et al. (2019) showed using a synthetic model that a large tolerance in magnetization intensity in early steps of the inversion for closely spaced bodies' gives erroneous results and creates local artifacts due to the high degree of freedom in the inversion process. Keeping the intensity fixed, or varying it in small steps, forces the magnetization directions to be uniform in areas of homogeneous intensity. Here, we used tolerance for the magnetization intensity of 10 A/m for the first inversion step and 300 A/m in the subsequent steps.

SMM acquisition profiles, with a total of 65,274 and of 65,527 data points, were used to invert NRM and AF100 scan data over the entire thin section, respectively. Isolated groups of anomalies from the selected subregions were inverted separately after interpolation of the SMM data and upsampling of the interpolated data along new profiles at an interval of 50 μm step. Data interpolation was made using a minimum
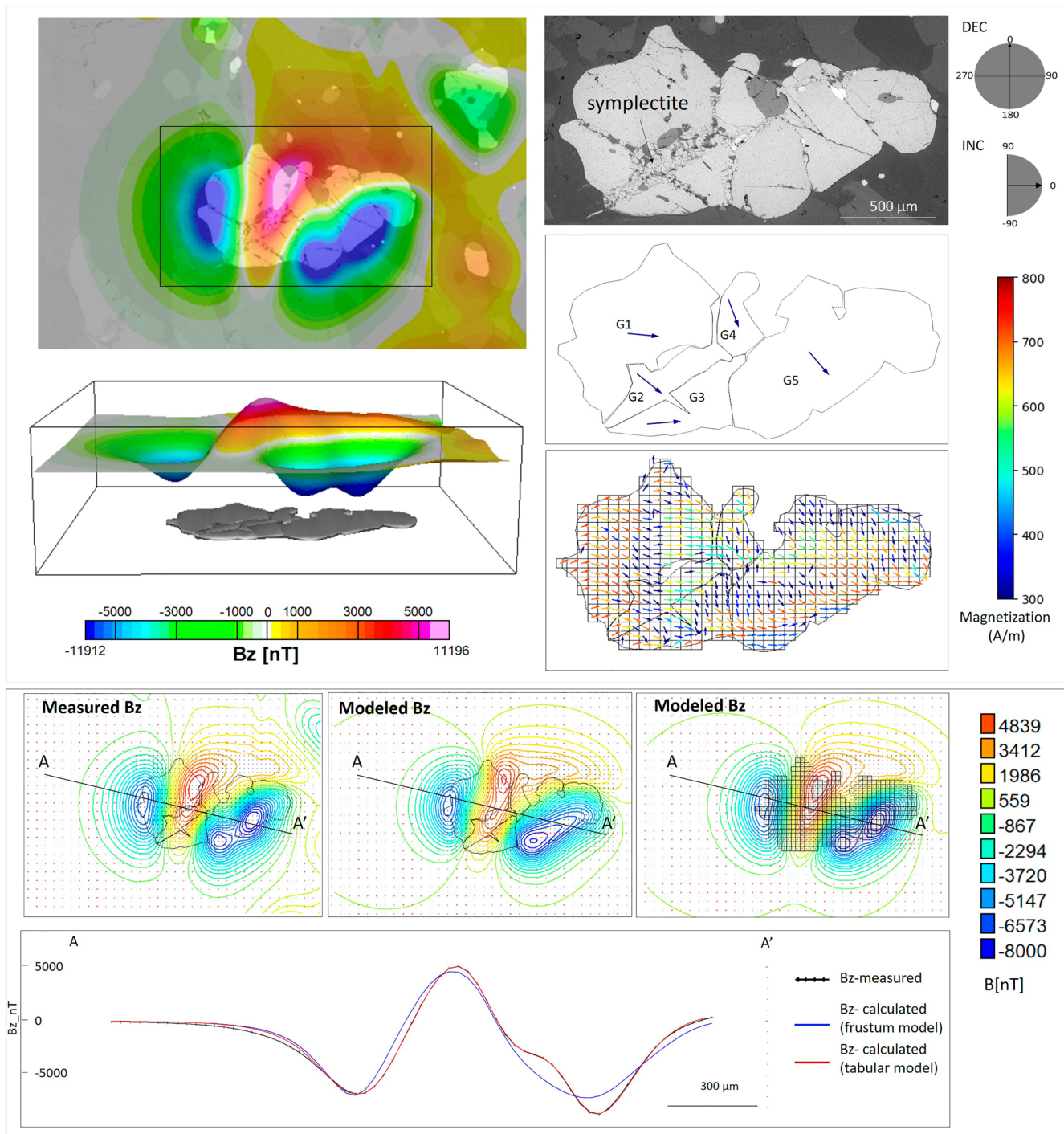
Figure 9. Left panel: map and 3D views of the magnetic anomaly measured over the grains from area 4 in Figure 4. Right panel: SEM images and frustum and tabular-body models of the grains (G1–G5) with arrows color coded by magnetization intensity and oriented according to inclination angle. G1 is titanohematite with abundant ilmenite exsolution lamellae with lower magnetization intensities in areas of hematite–rutile–spinel symplectite. Bottom panel: contour lines and profile with calculated and measured Bz for both frustum and tabular bodies. Red points on contour maps are data points where the Bz is calculated. SEM, scanning electron microscope.

curvature gridding algorithm, which is the smoothest possible surface to the data points (Briggs, 1974). For the gridding, we used a cell size of 25 μm, which is one fourth of the data sample interval. Other parameters controlling grid accuracy and coverage setting are (1) maximum number of iterations, set to 100,

(2) tolerance required for each grid cell set to a default of 0.1% of the range of the data, and (3) blanking distance, that is, how far the grid is extrapolated away from the nearest data point, set to 110 µm.

3. Magnetic Inversion Results

3.1. Inversion Results on the NRM Magnetic Scan Data

3.1.1. Full Scan Inversion With Frustum Bodies

Magnetic data inversions with frustum bodies gave reasonable fit to the measured data with a root mean square error (RMS) of 1.2% calculated over a total of 65,274 data points. The RMS is the root mean square difference between measured and calculated data, normalized by the measured data range. A total of 261 frustum bodies were used to model the titanohematite and hematite grains. Inversions of frustum bodies assume a homogeneous magnetization for each body. The magnetization for each modeled grain ranges from 12 to 785 A/m (Figure 5(b)). Grains with distinctly weaker or stronger magnetic anomalies were examined in detail in reflected light and by SEM microscopy. We found that the grains with weak magnetization are millimeter size MD hematite, with little-to-no ilmenite exsolution, while those with high magnetization show abundant ilmenite exsolution lamellae. Furthermore, some titanohematite grains modeled using single frustum bodies are composite titanohematite grains. Modeled grains are surrounded by paramagnetic silicates. We inferred a background of zero magnetization in the silicate area outside the modeled grains. Although smaller opaque minerals may occur in the silicate, the FORC diagram indicates that the component of magnetization attributable to high-M_s phases that might contribute to the total response despite small particle volumes, for example, single-domain magnetite, is negligible.

The resultant bulk magnetization of composite magnetic grains could be weakened by internal inhomogeneities due to the different orientations of the magnetization (Robinson et al., 2013; Robinson, Heidelbach, et al., 2006). The variation in magnetization inclination and declination angles are shown on the rose diagram in the stereonet in Figure 5(c). The rose diagram has a bin size of 10° and indicates a higher frequency on the circular distribution of grains magnetization directions in the SW quadrant of the plot. The direction of the total moment calculated by vector sum of all individual grains moments has an Inc of 6.8° and a Dec of 237°. In the x, y coordinate system of the thin section (Figure 4), declination angles are calculated assuming north parallel to the y axis.

3.1.2. Subregions Inversion With Tabular Bodies

While frustum bodies provide a "bulk" magnetization for each isolated grain, to investigate internal magnetic structure, tabular bodies with surface areas of 50×50 µm were used to discretize the volume of the grains. Given the resolution of the measured data, internal variation may be considered reliable over areas of 200×200 µm. Figure 6 shows models with frustum and tabular bodies of an isolated grain (area 1). This titanohematite grain contains abundant exsolution lamellae of ilmenite and pyrophanite and exsolution of rutile needles and spinel. The grain correlates with a positive magnetic anomaly with peak intensity of ≈4,500 nT, and the shape of the anomaly suggests that the grain is magnetized normal to the sample plane. A BSE image of the grain shows that the dominant ilmenite microstructure can be observed in different directions, indicating that a grain boundary exists and that this grain is composite. This observation matches with the tabular-body model results in which the magnetization is not homogeneous across the grain but varies in intensity and orientation. A SW-NE oriented profile shows the discrepancies between the modeled and the measured data for the frustum and tabular-body models. The frustum body has a larger mismatch to the data due to the approximation of a homogeneous magnetization for the entire grain (Figure 6). The tabular-body model allows a better fit of the measured data, though produces uncertain results at the edge of the grains (Pastore et al., 2019). Tabular bodies with larger magnetization intensities at the edge are considered less reliable. However, the average magnetization calculated by vector averaging the modeled tabular bodies magnetizations is of the same order of magnitude as that calculated from the frustum-body inversion (Table 1).

In area 2, models of both frustum and tabular bodies correlate with a negative magnetic anomaly of 6080 nT (Figure 7). This is a composite titanohematite grain with fine exsolution lamellae of ilmenite and pyrophanite, and spinel grains. Internal to the grain are symplectites of hematite, rutile, and spinel, earlier described

Table 1
Vector Average Magnetization From Frustum and Tabular Models for Grains From Selected Areas Calculated After Inversion of the NRM Scan Data

Modeled area	Grain	Volume ($\times 10^6$ μm^3)	Frustum model				Tabular model			
			Int	Decl	Incl	RMS[a]	Int	Decl	incl	RMS[a]
Area 1	G1	4.83	244	343	56		4.7	357	69	
Area 2	G1	6.82	277	40	−78	5.6	423	244	−79	1.8
Area 3	G1	40.76	12	80	−2	4.2	26	264	−6	1.8
	G2	1.98	267	197	13		161	223	55	
	G3	8.27	47	201	68		65	211	6	
	G4	1.75	50	205	5		159	242	−9	
	G5	10.11	235	302	−40		186	274	−40	
	G6	0.30	620	217	42		308	272	37	
	G7	0.66	468	280	73		299	249	56	
	G8	0.22	500	118	40		220	238	82	
Area 4	G1	10.17	479	266	−2	5	477	272	−11	2.1
	G2	2.95	380	251	−9		380	241	−11	
	G3	3.41	369	86	−5		240	182	−28	
	G4	1.96	441	231	−67		442	206	−48	
	G5	14.71	380	245	−9		398	191	−43	
Area 5	G1	8.08	668	291	−33	4.5	693	250	−28	1.9
Area 6	G1	7.23	474	233	2	8.1	533	245	2	1.3
	G2	8.80	186	318	24		181	293	73	
Area S1	G1	3.09	502	137	84	5.8	705	322	73	0.9
Area S2	G1	1.43	158	302	51	3.5	246	298	58	0.7
	G2	4.92	267	296	81		347	294	81	
Area S3	G1	2.23	544	235	83	7.2	873	280	85	2
Area S4	G1	5.07	310	127	−25	2.7	347	299	−25	1.1
	G2	9.35	452	237	−12		363	239	0	
	G3	3.29	398	118	10		311	337	21	
	G4	6.63	446	294	67		443	323	74	

Note. Modeled areas localities are shown in Figure 4.

[a]RMS error calculated over selected areas for frustum and tabular models. RMS values for frustum bodies are larger than those for the tabular-body models. Note that RMS values for models with frustum bodies over discrete areas are above 2%; however, the value calculated over the entire thin section model, with all frustum bodies, is below 2%.

by McEnroe and Brown (2000). Two frustum models of the grain were tested: one using a single body and a second using two bodies for the upper and lower part of the grain (see dashed red line on single frustum model in Figure 7, which traces a mineral grain boundary). For the latter, data inversion gives slightly different intensities for the magnetization (360 and 306 A/m) of the two frustum bodies and different directions (Decl/Inc: 062°/−66° for the upper part and 220°/−65° for the lower part). The improvement of RMS values from 5.6% for a single body to 4.0% for two frustum bodies, to 1.8% for the tabular-body model, suggests that the magnetization is not homogeneous across the grain with variability in intensity and orientation. A profile shows the discrepancies between the modeled data and the measured data for the frustum and tabular-body models. There is a good agreement between the measured and the calculated data for both frustum and tabular models. Single frustum and tabular-body average magnetizations are listed in Table 1 for comparison.

Areas with larger grains, and/or closely spaced grains, were also modeled with tabular bodies. Modeled grain from area 3 is shown in Figure 8. The oxide mineralogy in the area consists of a large 2-mm-wide hematite grain without ilmenite exsolution and smaller exsolved titanohematite grains. The hematite grain (G1) has a much weaker magnetic signature compared to the nearby titanohematite grains. The measured fields across this area in the NRM scan ranges from approximately −300 to 300 nT, and the grain has a magnetization intensity of 12 A/m, calculated with a frustum model. The large titanohematite grain on the south-east corner correlates with a predominantly negative magnetic anomaly peaking at −7,000 nT (Figure 8). Inversion results are consistent with these observations, with weaker magnetization intensities in the hematite grain (G1) and stronger intensities in the titanohematite grains (G2–G8). The frustum-body magnetizations and the vector average magnetization calculated from tabular bodies for each grain are listed in Table 1. The weak magnetization calculated for grains G3 and G4 illustrates the ambiguity inherent in inversion results when magnetic sources are closely spaced. The presence of a small amount of nonmagnetic chlorite (dark gray color in SEM image in Figure 8) inside the titanohematite suggests that the total moment of the grain may indeed be lower than others that do not show this alteration. In addition, the magnetic fields generated by G3 and G4 are partially canceled by those from the neighboring grains, yielding a lower calculated magnetization for G3 and G4 than would be obtained if they were isolated. Without additional constraints, the validity of either of these two interpretations cannot be distinguished. The development of inversion techniques for closely spaced sources to address this nonuniqueness is the focus of ongoing research within our group.

Modeled area 4 has a complex mineralogical assemblage with details shown in Figure 9. The assemblage consists of titanohematite grains and internal symplectites of hematite, rutile, and spinel. These multiple grains result in a complex magnetic anomaly with two magnetic lows up to −8,610 nT bounding a magnetic high with a peak amplitude of ≈6,150 nT. To model the grains, we used 5 frustum bodies and a total of 463 tabular bodies. Inversion results on both frustum and tabular bodies suggest an heterogeneous magnetization with higher intensities over the exsolved titanohematite and lower magnetization intensities over the areas of the hematite–rutile–aluminum spinel symplectites.

3.2. Inversion Results on Magnetic Scan Data After AF Demagnetization

3.2.1. Full Scan Inversion With Frustum Bodies

Inversions on frustum bodies were also run on the AF scan data. To compute the change in measured Bz after AF demagnetization of the sample, we subtract the NRM scan from the AF scan after upward continuation of the NRM scan to the same sensor elevation of the AF scan (Figure 10). Overall, the magnetic anomalies mapped before and after AF demagnetization retain similar shapes. However, grains with more complex structures than the isolated single grains showed a larger change in Bz.

The same frustum bodies used to model the entire thin section and invert for the NRM data were also used to model the Bz data measured after AF demagnetization. The calculated data gave reasonable fit to the measured magnetic data with a RMS of 1.4%. The magnetization for modeled grains ranges from 18 to 792 A/m (Figure 11) with highest intensities in smaller grains (volumes below 3×10^5 μm³). Magnetization directions (Inc and Dec angles) vary across the sample as shown on the stereonet in Figure 11(c). Nevertheless, the diagram in Figure 11(c), with bin size of 10°, indicates a higher frequency on the circular distribution of grains magnetization directions in the SW quadrant of the plot, similar to that in Figure 5(c). The direction of the total moment calculated by vector sum of all individual grains moments has an Inc of 11° and a Dec of 233°.

3.2.2. Subregions Inversion With Tabular Bodies

To investigate further the change in the field response after AF demagnetization, grains were also modeled with tabular bodies; two modeled areas are shown in Figures 12 and 13. Modeled area 5 includes a titanohematite grain with fine exsolution which correlates with a wide range in Bz values (from −11,760 to 6,720 nT, Figure 12(a)). Inversion results on the single frustum body, and on the tabular bodies show 20%–50% decrease in the magnetization intensity of the modeled magnetic source after AF demagnetization with little change in the magnetization direction (Figure 12(b)). A profile across the modeled area shows the match
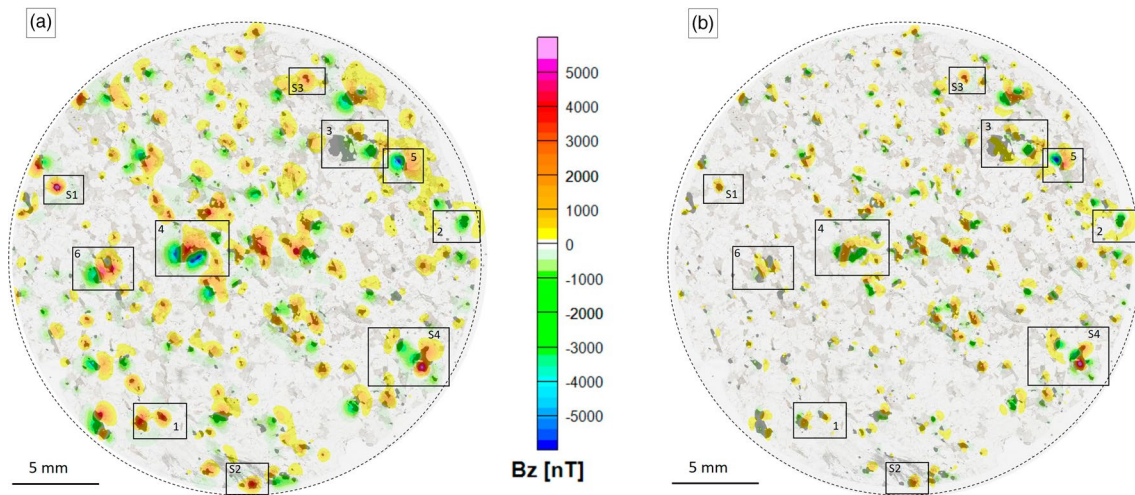
Figure 10. (a) Overlay of scan data measured after demagnetization of the sample (AF_Bz) and optical photograph of the sample. (b) Overlay of the residual grid (NRM_Bz minus AF_Bz) calculated by subtracting the magnetic scan made before and after demagnetizing the sample. The two magnetic scans had 3 μm sensor elevation difference, we therefore upward continued the NRM_Bz data to the same sensor elevation as AF_Bz before subtraction. AF, alternating field; NRM, natural remanent magnetization.

between the modeled and calculated Bz for the two models with tabular bodies before and after demagnetization (Figure 12(d)). To visualize changes in these two models, we calculated the Euclidean distance between modeled magnetization vectors of each tabular body in the NRM and AF100 models (Figure 12(c)). A larger Euclidean distance indicates larger deviations of the two vectors, and therefore a greater change in the magnetization; we observed larger Euclidean distances after demagnetization over the lower part of the modeled source, which corresponds to a change in the titanohematite microstructure.

The second modeled area (area 6, in Figure 4) includes two large titanohematite grains (G1–G2) surrounded by smaller grains (Figure 13). The measured field across this area in the NRM scan ranges between −4,060 and 6,670 nT with local weakening over G2 (Figure 13(a)). This area where the field approaches 0 results from the overlap of responses from the two larger titanohematite grains. An SEM image of the weaker zone shows a preferred orientation in the titanohematite lamellae and a clear grain boundary between this zone and the surrounding titanohematite (red dotted line in Figure 13(c)). The G1 exsolution lamellae are mostly oriented NW-SE and the smaller grain at the southern edge is rimmed by spinel. Both frustum and tabular bodies models suggest a reduction in the magnetization intensity after AF demagnetization of the sample (Figure 13(b)). To visualize changes in these two titanohematite grains, we calculated the Euclidean distance between modeled magnetization vectors of each tabular body in the NRM and AF100 models (Figure 13(c)). The inversion results suggest a heterogeneous change after AF demagnetization in both G1 and G2, consistent with observations of changes in microstructure.

4. Discussion

Previous studies on the GMS rocks showed that these have a remarkable large and stable remanent magnetization (Balsley & Buddington, 1954; Brown & McEnroe, 2012) linked to the amount of fine exsolution lamellae in the titanohematite (Kasama et al., 2004; McEnroe & Brown, 2000). Here, we investigate the fine-scale magnetization of sample AD34-6b using SMM and presented the results of the inversion of SMM data acquired in near-field-free conditions, before and after AF demagnetization.

To compare directly the inversion results with the bulk magnetic properties of the thin section, we calculated the total moment obtained from the modeling of 261 individual grains in the thin section and compared it to the moment measured on the thin section in GSJ-Lab, AIST, with a 2G superconducting rock magnetometer (SRM). The inverse problem is inherently nonunique and can create solutions that fit the data but are not physically plausible. Comparison with an independent measurement of the total moment provides
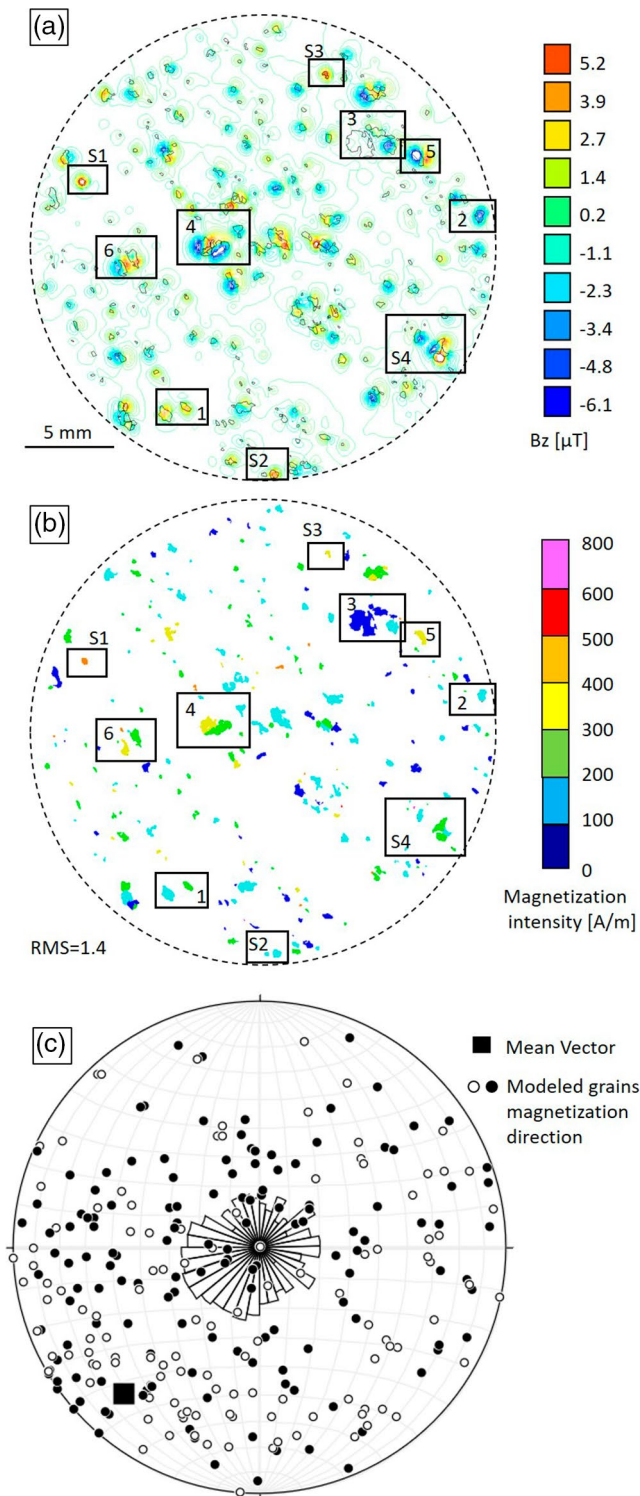
Figure 11. Data and inversion results after AF demagnetization. (a) Contour lines of the magnetic data with outline of the modeled grains (black box). (b) Bz full-scan inversion results with frustrum bodies color coded by magnetization intensity. (c) Stereoplot of magnetization direction for each of the 261 modeled bodies with 10° bin rose diagram in the middle. Closed circles indicate positive inclinations, open-negative inclinations, and the square indicates the standard mean vector direction of 20° inclination and 223° declination, calculated from all modeled grains by adding up the direction cosines of all of the individual unit vectors. AF, alternating field.
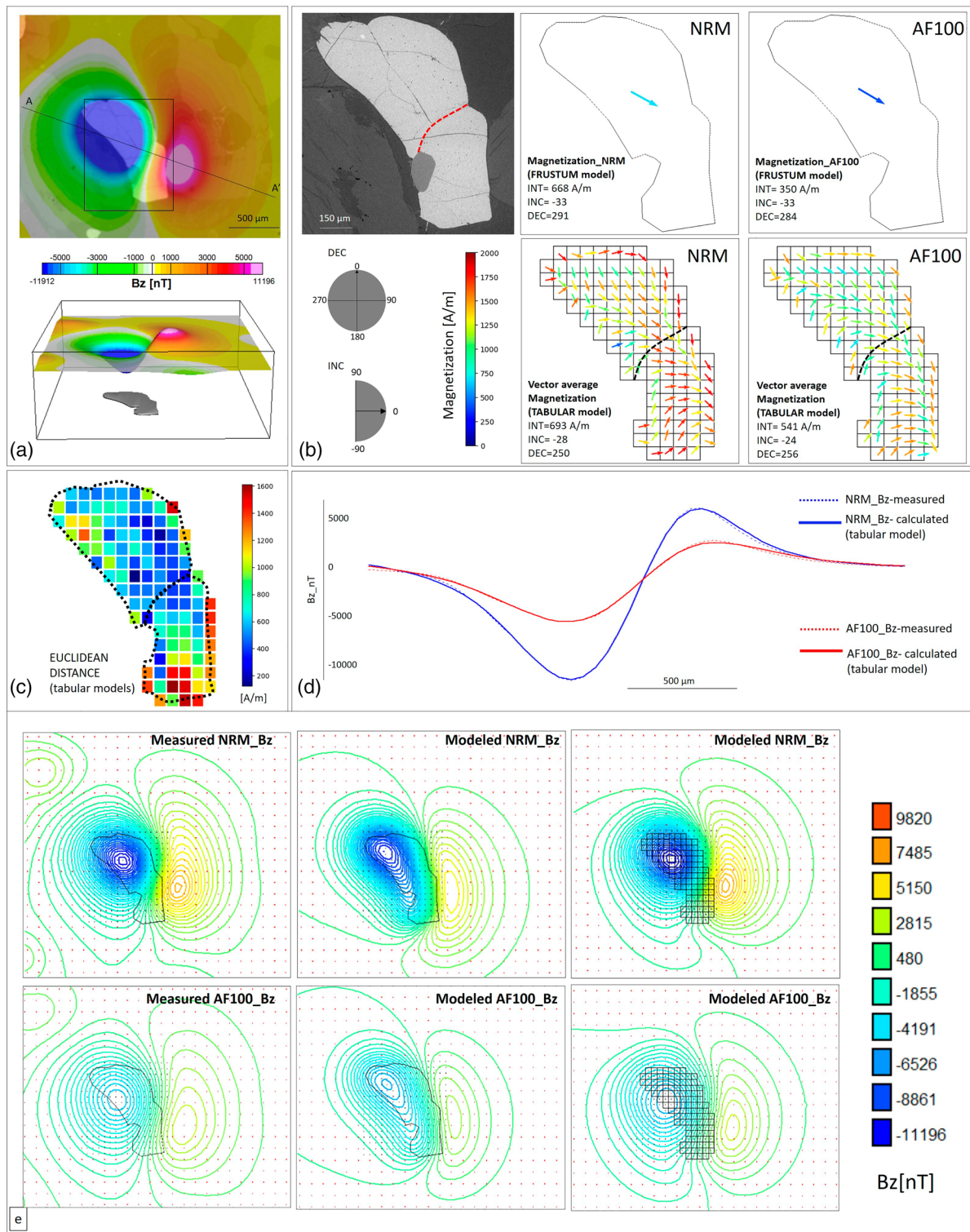
Figure 12. (a) Map and 3D views of the magnetic anomaly measured over the grains in area 5, Figure 4. (b) SEM image, and frustum and tabular models of the grain/grains obtained by inverting NRM_Bz and AF100_Bz scan data. The red dashed line on the SEM image indicates a grain boundary, traced based on the observation of a different orientation of the exsolution lamellae in two areas. Arrows on top of tabular bodies are color coded by magnetization intensity and oriented according to inclination angle. (c) Comparison of NRM and AF100 tabular-body models with each body colored according to the calculated Euclidian distance. (d) Profile AA′ (see Bz map in a for profile location) with modeled (tabular-body models) and calculated Bz for NRM and AF. (e) Contour lines and profile with calculated and measured Bz for NRM and AF both for frustum and tabular bodies. Red points on contour maps are data points where the Bz is calculated. SEM, scanning electron microscope; NRM, natural remanent magnetization; AF, alternating field.
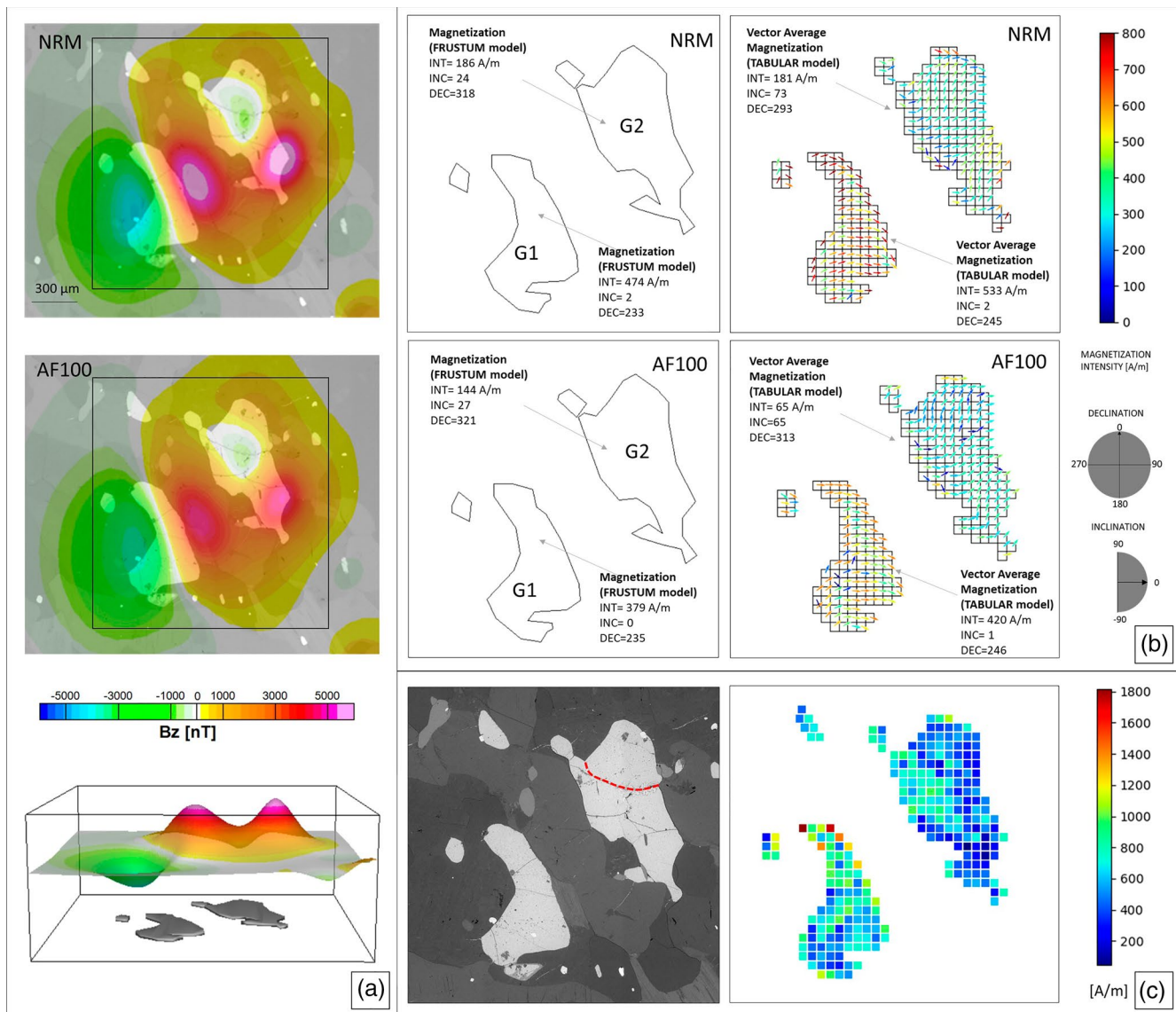
Figure 13. (a) Overlays of measured NRM_Bz and AF_Bz with the SEM image of area 6 (Figure 4), and 3D view of the NRM_Bz data and of the modeled titanohematite grains. (b) Frustum and tabular bodies models of the grains for both NRM and AF magnetic scan data with arrows color coded by magnetization intensity and oriented according to inclination angle. (c) Comparison of NRM and AF100 tabular-body models with each body colored according to the calculated Euclidian distance. NRM, natural remanent magnetization; AF, alternating field; SEM, scanning magnetic microscopy.

an important check on the inversion results and on the estimation of discrete grains magnetizations. To calculate the total moment, we applied a vector sum of the individual grains moments. The SRM moment for the thin section at the measured position was corrected from the raw moment values of the SRM in three axes using "effective length matrix" obtained by the *uresponse* software (Xuan & Oda, 2019) applied to the SRM in GSJ-Lab assuming uniform magnetization and a square flat plate with an area equivalent to the thin section. The calculated total moment from the inversion of the NRM_Bz scan data is 5.7×10^{-8} A m^2 and the moment measured with the SRM over the entire sample is 3.6×10^{-8} A m^2. The calculated total moment from the inversion of the AF_Bz scan data is 4.1×10^{-8} A m^2 and the measured moment is 3.8×10^{-8} A m^2. These values are in the same order of magnitude, which validates the approach used here.

We also used the calculated and the measured moments to calculate the bulk magnetization of the thin section assuming a sample volume of 1.52×10^{-8} m^3. This calculation gave values of 3.75 and 2.70 A/m for the magnetization of the model calculated from the NRM_Bz and AF100_Bz magnetic data, respectively. Mo-

ments measured with the SRM prior to and after AF demagnetization result instead in magnetization intensities of 2.4 and 2.5 A/m, respectively. The mismatch between the modeled and calculated values indicates that the modeled grain moments are overestimated. One reason for this mismatch is the capability of the SMM to discern small particles. Grains with volumes below 1.2×10^6 μm^3 consistently yielded magnetization values that were greater than those calculated for larger particles. Another reason for the discrepancy between the modeled and the measured moment is the nonnegligible area of the sensor and the consequent convolution effect on the data. Specifically, convolution can broaden the region of high magnetic response over small particles and result in an overestimation of the magnetic moment. In the future, deconvolution might be conducted together with modeling to improve the moment estimates and the sensor response, particularly over small particles. An additional source of error is the distance between modeled grains and magnetic sensor, here assumed to be constant; if the distance is smaller than the true distance, this could result in an exaggerated moment. Furthermore, grains modeled with frustum bodies have more complex magnetization structures, which prevent a perfect fitting of the measured and the modeled data. This mismatch and approximation of the magnetic minerals with simple bodies will affect the total moment. Nevertheless, given the spatial resolution of the data and modeling approximations, and based on the knowledge of the bulk response of companion specimens of this sample, we consider that the inversion results are well within the expected results.

Further, the bulk magnetization direction measured with the SRM instrument yield values (Inc = 20° and Dec = 223°) consistent with that calculated from our NRM scan model (Inc = 7° and Dec = 237°). Values are in the same coordinate system used for modeling of the data, with the x–y plane parallel to the sample surface and z positive downward. The inclination modeled from SMM of the thin section also matches well with that of the 2.5 cm core from which it was made. The azimuth was not preserved when the thin section was made and hence the declination cannot be compared. However, assuming z positive downwards, the AD34-6b paleomagnetic core inclination in unrotated specimen coordinates is 11.8° (see Table S1 in supplemental material for geographic and specimen coordinates of the paleomagnetic core), which compares well with the value obtained by inversion.

The inversion results suggest a consistent decrease in the magnetization intensity after AF demagnetization with only a minor change in magnetization directions (Figure 14). Declination and inclination angles of the modeled bodies' magnetizations are shown on a stereonet to compare modeling results before and after AF demagnetization (Figure 14(a)). The stereoplot shows scattered magnetization directions for both NRM and AF100 models, which do not cluster for subset ranges of grain size or magnetization intensity. However, the mean directions, calculated both using the Stereonet 10.0 program (Allmendinger et al., 2012; Cardozo & Allmendinger, 2013) and by vector averaging all modeled magnetizations, are consistent (Figure 14(a)). The mean direction calculated by summing the direction cosines of the individual unit vectors obtained by inversion of the NRM_Bz data was 219° declination and 12° inclination. The model obtained from the inversion of the AF_Bz data gave a similar mean vector direction with 223° declination and 20° inclination (Figure 14). These mean directions are consistent with those calculated by vector summation of moments of all individual grains (see Table S1 in Supplemental material for comparison). Magnetization directions of grains from selected areas discussed above are displayed on a stereonet in Figure 14(b). The latter shows that closely spaced grains contributing to more complex anomalies (e.g., grains from areas 3, 4, and S4) show variable directions, and plot toward shallower inclinations than those from selected isolated grains (e.g., grains from areas 1, 2, S1, and S3). Furthermore, we observed that grains from more complex magnetic anomalies also show larger changes in the magnetization direction after AF demagnetization (see length arrows in Figure 14(b)). This could be partly due to the uncertainty in the modeling of closely spaced particles with different magnetization. Closely spaced sources can indeed generate overlapping anomalies and prevent the correct estimation of individual particles magnetization; grains from area 6 (Figure 13) provide a good example (see supplemental material Figure S5) of this effect.

To compare the changes in magnetization direction after the AF demagnetization of individual grains, we calculated the cosine of the angle (cosine similarity) between respective modeled magnetizations before and after AF demagnetization. The cosine similarity is equal to one when the two vectors have same directions, zero if perpendicular, and negative one if the vectors are antiparallel (Pastore et al., 2019). As shown in the stereoplots, these directions are consistent with little deviation after AF demagnetization (Figure 14(c)). Comparison of inversion models of NRM_Bz and AF_Bz scan data shows that the modeled grains lose their
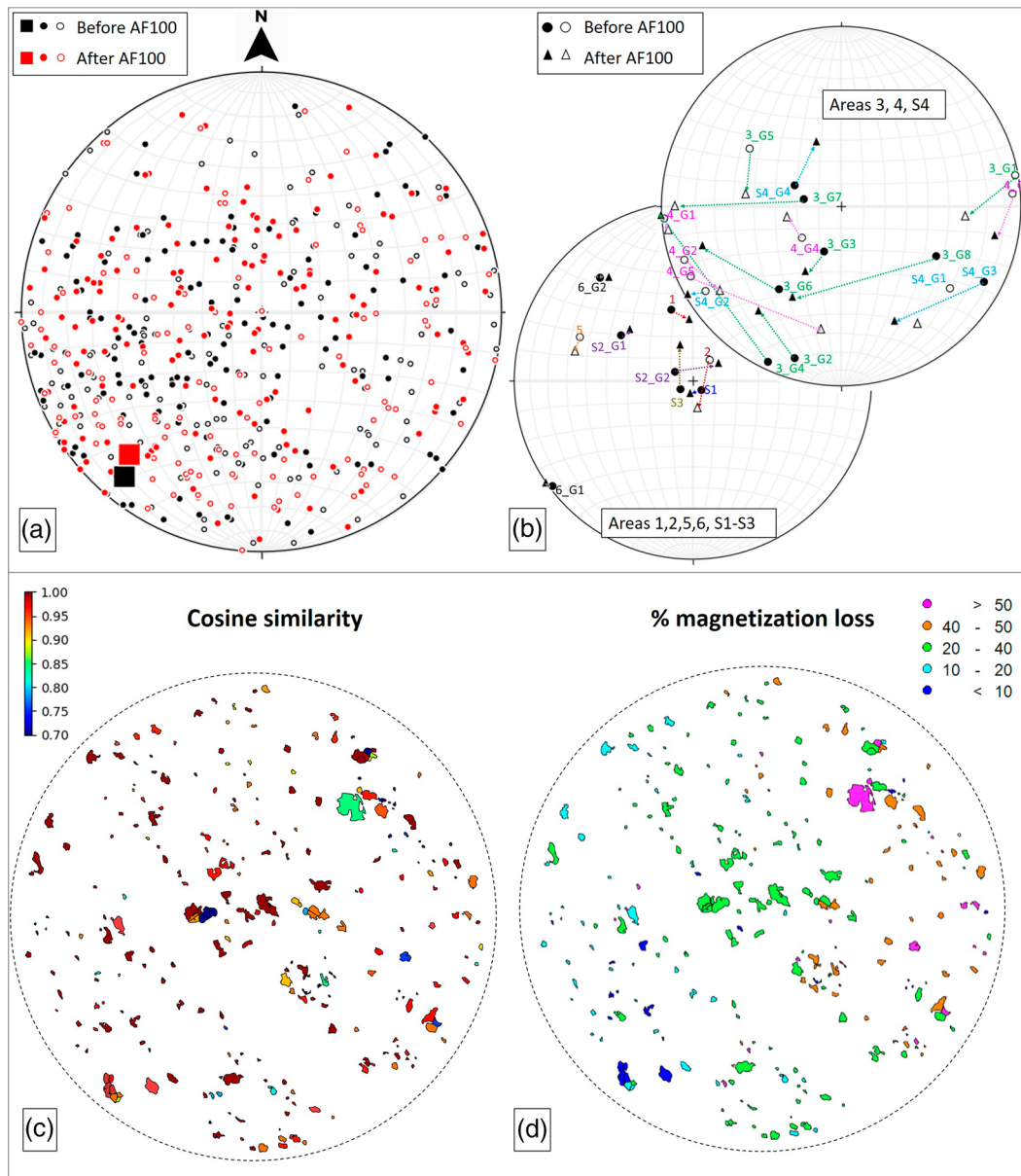
Figure 14. (a) Stereoplot of magnetization direction for modeled body before (black) and after (red) AF demagnetization. Closed circles, positive inclinations; open circles, reversed. Larger circles, mean vector direction for NRM, and AF100, calculated from all modeled grains. (b) Simplified stereoplots of Inc and Dec of grains modeled from selected areas (see Table 1). (c) Map view of the sample with modeled grains color coded according to cosine similarity between modeled magnetization before and after AF demagnetization. (d) Map view with outline of modeled grains and color coded by the percentage of magnetization lost (from <10% to >50%) after AF demagnetization of the sample. AF, alternating field; NRM, natural remanent magnetization.

initial intensity differently (Figure 14(d)). Grains that lost more than 50% of their NRM magnetization have volumes below $1.2 \times 10^6 \ \mu m^3$ or had weaker magnetization intensities in the NRM state (<50 A/m).

A plot of NRM and AF magnetization intensities of each body shows that grains with volumes below $1.2 \times 10^6 \ \mu m^3$ commonly deviate from the general linear trend (Figure 15). One reason could be the limitation imposed by the resolution of the data, acquired with a step size of 100 μm along x and y direction. Approximately 70% of the samples show a standard deviation from the best linear approximation ($y = 0.7085x$) of ±50 A/m. We also observed deviations from the linear trend for composite grains' particles. This deviation could be partly explained by uncertainties due to overlapping anomalies. The plot, based on the linear trend,
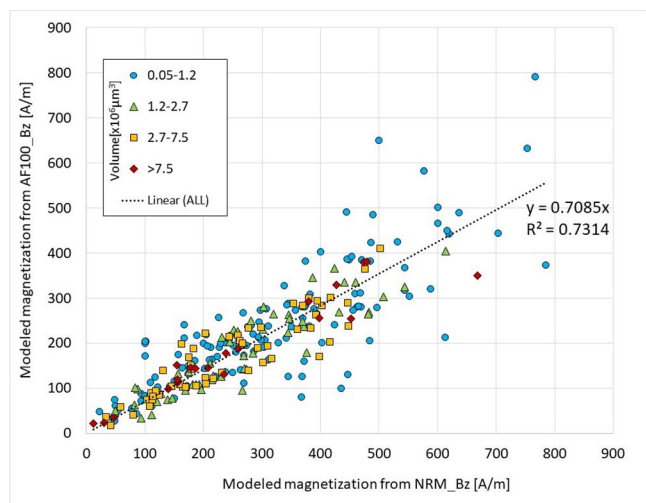
Figure 15. Plot of magnetization intensities of each frustum body calculated after inversion of the magnetic scan data before (NRM_Bz) and after (AF_Bz) demagnetization. Each circle indicates one body and is color coded by grain volume. The trend line (black dotted line) shows the best linear fit of the modeled grains magnetization data. The coefficient of determination R^2 value is 0.7314 and indicates a rather good fit of the line to the data. This value increases to 0.83 when data from grains with volumes below 1.2×10^6 μm^3 are not included. NRM, natural remanent magnetization; AF, alternating field.

indicates that approximately 30% of the magnetization is lost after AF demagnetization. The AF demagnetization data from the seven core samples from this site showed only a minor change in remanence direction and a small decay in original NRM intensities (Brown & McEnroe, 2012). We must consider that the thin section is 0.12% the volume of a standard 1-in. core, and therefore is not fully representative of a complete paleomagnetic specimen.

5. Conclusions

- SMM was used to investigate the bulk magnetic response of sample AD34-6b and to identify the mineralogical sources of the high and stable NRM in the RB microcline–sillimanite gneiss.
- The magnetization of AD34-6 is dominated by exsolved titanohematite with abundant lamellae, and only negligible contributions from other phases. The titanohematite exhibits M_{rs}/M_s values of 0.66 and high coercivity, with almost no switching occurring at fields less than 100 mT and a component of magnetization with coercivity greater than 1.1 T. The M_s of the titanohematite is 0.58 A m^2/kg, an enhancement of 40%–100% above single-phase hematite values, which originates from the interface moment of the ilmenite lamellae with the titanohematite host. The FORC and remanent Preisach maps show high-coercivity, shifted signals that are typical of hematite which may result from its hexagonal magnetocrystalline anisotropy with additional contributions from the exchange-coupled interface moments of the ilmenite lamellae with the titanohematite host.
- Mapping by SMM confirms that the exsolved titanohematite grains are the sources of the magnetic anomalies, which dominate the bulk magnetic response. Inversion results and SEM observations confirm the effect of high coercivity resulting from the microstructure in the titanohematite on the local magnetic properties.
- Modeling of the thin section magnetic scans determined the remanent magnetization direction and intensities of the discrete magnetic mineral sources within the sample before and after AF demagnetization of the thin section to 100 mT.
- The magnetization directions of discrete modeled grains are scattered; however, the mean directions are consistent with the bulk average directions measured on this sample, and from companion specimens from site AD34. Furthermore, we observed a consistent average direction before and after AF demagnetization of the sample, which confirms the high magnetic stability of the titanohematite. Inversion results suggest that approximately 30% of the initial magnetization intensity of individual grains is lost with AF demagnetization to 100 mT. This value is consistent with the loss of bulk magnetization calculated from the thin section models before (3.75 A/m) and after (2.70 A/m) demagnetizing the thin section.
- Vector moment calculations from the NRM scan model of the sample are consistent with the values measured with the moment magnetometer. Mismatch between the calculated and measured moment are interpreted to be caused by overestimates in the magnetization intensities of modeled particles with volumes below 10^6 μm^3. Calculated and measured bulk magnetization directions are also consistent.
- Calculated magnetization for the entire thin section from the NRM and AF models is well within the range of the bulk magnetizations measured on paleomagnetic cores from site AD34.

Data Availability Statement

Data sets for this research are available at https://dataverse.no/dataset.xhtml?persistentId=doi:10.18710/OGQWZM#. Additional figures with inversion results on other areas of the sample (Figures S1–S5) and a table (Table S1) with measured and calculated mean magnetization directions of the sample are provided in the supplemental material file.

References

Allmendinger, R. W., Cardozo, N., & Fisher, D. (2012). *Structural geology algorithms: Vectors and tensors in structural geology*. Cambridge University Press.

Balsley, J. R., & Buddington, A. F. (1954). Correlation of reverse remanent magnetism and negative anomalies with certain minerals. *Journal of Geomagnetism and Geoelectricity*, *6*(4), 176–181.

Balsley, J. R., & Buddington, A. F. (1957). Remanent magnetism of the Russell Belt of gneisses, northwest Adirondack Mountains, New York. *Advances in Physics*, *6*(23), 317–322.

Balsley, J. R., & Buddington, A. F. (1958). Iron-titanium oxide minerals, rocks, and aeromagnetic anomalies of the Adirondack area, New York. *Economic Geology*, *53*(7), 777–805.

Bickford, M. E., McLelland, J. M., Selleck, B. W., Hill, B. M., & Heumann, M. J. (2008). Timing of anatexis in the eastern Adirondack Highlands: Implications for tectonic evolution during ca. 1050 Ma Ottawan orogenesis. *The Geological Society of America Bulletin*, *120*, 950–961.

Blakely, R. J. (1996). *Potential theory in gravity and magnetic applications*. Cambridge University Press.

Bohlen, S. K., Valley, J., & Essene, E. (1985). Metamorphism in the Adirondacks: I. Petrology, pressure, and temperature. *Journal of Petrology*, *26*, 971–992.

Briggs, I. C. (1974). Machine contouring using minimum curvature. *Geophysics*, *39*(1), 39–48.

Brown, L. L., & McEnroe, S. A. (2008). Magnetic properties of Anorthosites: A forgotten source for planetary magnetic anomalies? *Geophysical Research Letters*, *35*, L02305. https://doi.org/10.1029/2007GL032522

Brown, L. L., & McEnroe, S. A. (2012). Paleomagnetism and magnetic mineralogy of Grenville metamorphic and igneous rocks, Adirondack Highlands, USA. *Precambrian Research*, *212*, 57–74. https://doi.org/10.1016/j.precamres.2012.04.012

Brownlee, S. J., Feinberg, J. M., Kasama, T., Harrison, R. J., Scott, G. R., & Renne, P. R. (2011). Magnetic properties of ilmenite–hematite single crystals from the Ecstall pluton near Prince Rupert, British Columbia. *Geochemistry, Geophysics, Geosystems*, *12*, Q07Z29. https://doi.org/10.1029/2011GC003622

Buddington, A. F., & Leonard, B. F. (1962). *Regional geology of the St. Lawrence county magnetite district, northwest Adirondacks, New York* (No. 376). US Government Printing Office.

Cardozo, N., & Allmendinger, R. W. (2013). Spherical projections with OSXStereonet: *Computers & Geosciences*, *51*, 193–205. https://doi.org/10.1016/j.cageo.2012.07.021

Church, N. S., Fabian, K., & McEnroe, S. A. (2016). Nonlinear Preisach maps: Detecting and characterizing separate remanent magnetic fractions in complex natural samples. *Journal of Geophysical Research: Solid Earth*, *121*, 8373–8395. https://doi.org/10.1002/2016JB013465

Church, N. S., & McEnroe, S. A. (2018). Magnetic field surveys of thin sections, *Australian Society of Exploration Geophysicists Extended Abstracts*, *2018*(1), 1–5. https://doi.org/10.1071/ASEG2018abW10_3F

Clark, D. A. (1999). Magnetic petrology of igneous intrusions: Implications for exploration and magnetic interpretation. *Exploration Geophysics*, *30*(1–2), 5–26. https://doi.org/10.1071/EG999005

Egli, R. (2013). VARIFORC: An optimized protocol for calculating non-regular first-order reversal curve (FORC) diagrams. *Global and Planetary Change*, *110*, 302–320. https://doi.org/10.1016/j.gloplacha.2013.08.003

Egli, R., & Heller, F. (2000). High-resolution imaging using a high-Tc superconducting quantum interference device (SQUID) magnetometer. *Journal of Geophysical Research*, *105*(B11), 25709–25727.

Fabian, K. (2003). Some additional parameters to estimate domain state from isothermal magnetization measurements. *Earth and Planetary Science Letters*, *213*(3–4), 337–345. https://doi.org/10.1016/S0012-821X(03)00329-7

Ferré, E. C., Kupenko, I., Martín-Hernández, F., Ravat, D., & Sanchez-Valle, C. (2021). Magnetic sources in the Earth's mantle. *Nature Reviews Earth & Environment*, *2*, 59–69. https://doi.org/10.1038/s43017-020-00107-x

Hankard, F., Gattacceca, J., Fermon, C., Pannetier-Lecoeur, M., Langlais, B., Quesnel, Y., et al. (2009). Magnetic field microscopy of rock samples using a giant magnetoresistance-based scanning magnetometer. *Geochemistry, Geophysics, Geosystems*, *10*, Q10Y06. https://doi.org/10.1029/2009GC002750

Harrison, R. J., & Feinberg, J. M. (2008). FORCinel: An improved algorithm for calculating first-order reversal curve distributions using locally weighted regression smoothing. *Geochemistry, Geophysics, Geosystems*, *9*, Q05016. https://doi.org/10.1029/2008GC001987

Harrison, R. J., Zhao, X., Hu, P., Sato, T., Heslop, D., Muxworthy, A. R., et al. (2019). Simulation of remanent, transient, and induced first-order reversal curve (FORC) diagrams for interacting particles with uniaxial, cubic, and hexagonal anisotropy. *Journal of Geophysical Research: Solid Earth*, *124*, 12404–12429. https://doi.org/10.1029/2019JB018050

Kasama, T., Dunin-Borkowski, R. E., Asaka, T., Harrison, R. J., Chong, R. K., McEnroe, S. A., et al. (2009). The application of Lorentz transmission electron microscopy to the study of lamellar magnetism in hematite–ilmenite. *American Mineralogist*, *94*, 262–269. https://doi.org/10.2138/am.2009.2989

Kasama, T., McEnroe, S. A., Ozaki, N., Kogure, T., & Putnis, A. (2004). Effects of nanoscale exsolution in hematite–ilmenite on the acquisition of stable natural remanent magnetization. *Earth and Planetary Science Letters*, *224*(3–4), 461–475. https://doi.org/10.1016/j.epsl.2004.05.027

Kawai, J., Oda, H., Fujihira, J., Miyamoto, M., Miyagi, I., & Sato, M. (2016). SQUID microscope with hollow-structured cryostat for magnetic field imaging of room temperature samples. *IEEE Transactions on Applied Superconductivity*, *26*(5), 1–5.

Levenberg, K. (1944). A method for the solution of certain non-linear problems in least squares. *Quarterly of Applied Mathematics*, *2*(2), 164–168. https://doi.org/10.1090/qam/10666

Lima, E. A., & Weiss, B. P. (2016). Ultra-high sensitivity moment magnetometry of geological samples using magnetic microscopy. *Geochemistry, Geophysics, Geosystems*, *17*, 3754–3774. https://doi.org/10.1002/2016GC006487

Marquardt, D. (1963). An algorithm for least-squares estimation of nonlinear parameters. *Journal of the Society for Industrial and Applied Mathematics*, *11*(2), 431–441.

McCammon, C., McEnroe, S. A., Robinson, P., & Burton, B. P. (2009). High efficiency of natural lamellar remanent magnetisation in single grains of ilmeno-hematite calculated using Mössbauer spectroscopy, *Earth and Planetary Science Letters*, *288*, 268–278. https://doi.org/10.1016/j.epsl.2009.09.030

McEnroe, S. A., & Brown, L. L. (2000). A closer look at remanence-dominated aeromagnetic anomalies: Rock magnetic properties and magnetic mineralogy of the Russell Belt microcline–sillimanite gneiss, northwest Adirondack Mountains, New York. *Journal of Geophysical Research*, *105*(B7), 16437–16456. https://doi.org/10.1029/2000JB900051

McEnroe, S. A., Brown, L. L., & Robinson, P. (2009). Remanent and induced magnetic anomalies over a layered intrusion: Effects from crystal fractionation and recharge events. *Tectonophysics*, *478*, 119–134. https://doi.org/10.1016/j.tecto.2008.11.021

McEnroe, S. A., Fabian, K. Robinson, P., Giana, C. & Brown, L. L. (2009). Crustal magnetism, lamellar magnetism and rocks that remember. *Elements*, *5*, 241–246. https://doi.org/10.2113/gselements.5.4.241

McEnroe, S. A., Harrison, R., Robinson, P., Golla, U., & Jercinovic, M. J. (2001). Effect of fine-scale microstructures in titanohematite on the acquisition and stability of natural remanent magnetization in granulite facies metamorphic rocks, southwest Sweden: Implications for crustal magnetism. *Journal of Geophysical Research*, *106*(B12), 30523–30546. https://doi.org/10.1029/2001JB000180

McEnroe, S. A., Harrison, R. J., Robinson, P., & Langenhorst, F. (2002). Nanoscale hematite–ilmenite lamellae in massive ilmenite rock: An example of 'lamellar magnetism' with implications for planetary magnetic anomalies. *Geophysical Journal International*, *151*, 890–912. https://doi.org/10.1046/j.1365-246X.2002.01813.x

McEnroe, S. A., Robinson, P., Church, N., & Purucker, M. (2018). Magnetism at depth: A view from an ancient continental subduction and collision zone. *Geochemistry, Geophysics, Geosystems*, *19*, 1123–1147. https://doi.org/10.1002/2017GC007344

McEnroe, S. A., Robinson, P., Langenhorst, F., Frandsen, C., Terry, M. P., & Boffa Ballaran, T. (2007). Magnetization of exsolution intergrowths of hematite and ilmenite: Mineral chemistry, phase relations, and magnetic properties of hemo-ilmenite ores with micron- to nanometer-scale lamellae from Allard Lake, Quebec. *Journal of Geophysical Research*, *112*, B10103. https://doi.org/10.1029/2007JB004973

McEnroe, S. A., Robinson, P., Miyajima, N., Fabian, K., Dyar, D., & Sklute, E. (2016). Lamellar magnetism and exchange bias in billion-year-old titanohematite with nanoscale ilmenite exsolution lamellae: I. Mineral and magnetic characterization. *Geophysical Journal International*, *206*(1), 470–486. https://doi.org/10.1093/gji/ggw155

McEnroe, S. A., Robinson, P., & Panish, P. (2001). Aeromagnetic anomalies, magnetic petrology and rock magnetism of hemo-ilmenite- and magnetite-rich cumulates from the Sokndal Region, South Rogaland, Norway. *American Mineralogist*, *86*, 1447–1468. https://doi.org/10.2138/am-2001-11-1213

Michels, A., Fichler, C., Pastore, Z., & McEnroe, S. (2020). Magnetic mapping of fault zones in the Leka Ophiolite Complex, Norway. *Norwegian Journal of Geology*, *100*, 202003. https://doi.org/10.17850/njg100-1-1

Michels, A. C., McEnroe, S. A., & Fichler, C. (2018). Geophysical expression of the Leka Ophiolite, Norway modeled from integrated gravity, magnetic and petrophysical data. *Norwegian Journal of Geology*, *98*, 103–125. https://doi.org/10.17850/njg98-1-07

Muxworthy, A. R., King, J. G., & Heslop, D. (2005). Assessing the ability of first-order reversal curve (FORC) diagrams to unravel complex magnetic signals. *Journal of Geophysical Research*, *110*, B01105. https://doi.org/10.1029/2004JB003195

Nyquist, H. (1928). Certain topics in telegraph transmission theory. *Transactions of the American Institute of Electrical Engineers*, *47*(2), 617–644. https://doi.org/10.1109/T-AIEE.1928.5055024

Oda, H., Kawai, J., Miyamoto, M., Miyagi, I., Sato, M., Noguchi, A., et al. (2016). Scanning SQUID microscope system for geological samples: System integration and initial evaluation. *Earth Planets and Space*, *68*(179), 1–19. https://doi.org/10.1186/s40623-016-0549-3

Oda, H., Usui, A., Miyagi, I., Joshima, M., Weiss, B. P., Shantz, C., et al. (2011). Ultrafine-scale magnetostratigraphy of marine ferromanganese crust. *Geology*, *39*, 227–230. https://doi.org/10.1130/G31610.1

Oldenburg, D. W., & Pratt, D. A. (2007). Geophysical inversion for mineral exploration: A decade of progress in theory and practice. *Proceedings of Exploration*, *7*(5), 61–95.

Özdemir, Ö., & Dunlop, D. J. (2014). Hysteresis and coercivity of hematite. *Journal of Geophysical Research: Solid Earth*, *119*, 2582–2594. https://doi.org/10.1002/2013JB010739

Pastore, Z., Church, N. S., & McEnroe, S. A. (2019). Multistep parametric inversion of scanning magnetic microscopy data for modeling magnetization of multidomain magnetite. *Geochemistry, Geophysics, Geosystems*, *20*, 5334–5351. https://doi.org/10.1029/2019GC008542

Pastore, Z., McEnroe, S. A., ter Maat, G. W., Oda, H., Church, N. S., & Fumagalli, P. (2018). Mapping magnetic sources at the millimeter to micrometer scale in dunite and serpentinite by high-resolution magnetic microscopy. *Lithos*, *323*, 174–190. https://doi.org/10.1016/j.lithos.2018.09.018

Paterson, G. A., Zhao, X., Jackson, M. J., & Heslop, D. (2018). Measuring, processing, and analyzing hysteresis data. *Geochemistry, Geophysics, Geosystems*, *19*, 1925–1945. https://doi.org/10.1029/2018GC007620

Pratt, D. A., Foss, C. A., & Roberts, S. (2006). *User guided inversion & visualisation of interpretation confidence*. Paper presented at AESC Conference, Melbourne: Extended Abstract. Australian Earth Sciences Convention (AESC). http://www.tensor-research.com.au/home/further-reading

Purucker, M. E., &. Whaler, K. E. (2007). Crustal magnetism, In G. Schubert (Ed.), *Treatise on geophysics* (pp. 195–235), Amsterdam: Elsevier. https://doi.org/10.1016/B978-044452748-6.00091-2

Roberts, A. P., Heslop, D., Zhao, X., & Pike, C. R. (2014). Understanding fine magnetic particle systems through use of first-order reversal curve diagrams. *Reviews of Geophysics*, *52*, 557–602. https://doi.org/10.1002/2014RG000462

Robinson, P., Fabian, K., McEnroe, S. A., & Heidelbach, F. (2013). Influence of lattice-preferred orientation with respect to magnetizing field on intensity of remanent magnetization in polycrystalline hemo-ilmenite. *Geophysical Journal International*, *192*, 514–536. https://doi.org/10.1093/gji/ggs046

Robinson, P., Harrison, R. J., & McEnroe, S. A. (2006). Fe^{2+}/Fe^{3+} charge ordering in contact layers of lamellar magnetism: Bond valence arguments. *American Mineralogist*, *91*, 67–72. https://doi.org/10.2138/am.2006.2012

Robinson, P., Harrison, R. J., McEnroe, S. A., & Hargraves, R. (2002). Lamellar magnetism in the hematite–ilmenite series as an explanation for strong remanent magnetization. *Nature*, *418*, 517–520. https://doi.org/10.1038/nature00942

Robinson, P., Harrison, R. J., McEnroe, S. A., & Hargraves, R. (2004). Nature and origin of lamellar magnetism in the hematite–ilmenite series. *American Mineralogist*, *89*, 725–747. https://doi.org/10.2138/am-2004-5-607

Robinson, P., Heidelbach, F., Hirt, A. M., McEnroe, S. A., & Brown, L. L. (2006). Crystallographic–magnetic correlations in single crystal haemo-ilmenite: New evidence for lamellar magnetism. *Geophysical Journal International*, *165*, 17–31. https://doi.org/10.1111/j.1365-246X.2006.02849.x

Robinson, P., McEnroe, S. A., Miyajima, N., Fabian, K., & Church, N. (2016). Remanent magnetization, magnetic coupling, and interface ionic configurations of intergrown rhombohedral and cubic Fe-Ti oxides: A short survey, *American Mineralogist*, *101*(3), 518–530. https://doi.org/10.2138/am-2016-5519

Schrefl, T., Shoji, T., Winklhofer, M., Oezelt, H., Yano, M., & Zimanyi, G. T. (2012). First order reversal curve studies of permanent magnets. *Journal of Applied Physics*, *111*(7), 07A728. https://doi.org/10.1063/1.3678434

Shannon, C. E. (1948). A mathematical theory of communication. *The Bell System Technical Journal*, *27*(3), 379–423. https://doi.org/10.1002/j.1538-7305.1948.tb01338.x

Spear, F. S., & Markussen, J. C. (1997). Mineral zoning, P–T–X–M phase relations, and metamorphic evolution of some Adirondack granulites, New York. *Journal of Petrology*, *38*, 757–783.

Stoner, E. C., & Wohlfarth, E. P. (1948). A mechanism of magnetic hysteresis in heterogeneous alloys. *Philosophical Transactions of the Royal Society of London A: Mathematical, Physical and Engineering Sciences*, *240*(826), 599–642. https://doi.org/10.1098/rsta.1948.0007

ter Maat, G., Fabian, K., Church, N., & McEnroe, S. A. (2020). Separating geometry- from stress-induced remanent magnetization in magnetite with ilmenite lamellae from the Stardalur basalts, Iceland. *Geochemistry, Geophysics, Geosystems*, *21*, e2019GC008761. https://doi.org/10.1029/2019GC008761

ter Maat, G., McEnroe, S. A., Church, N., & Larsen, R. B. (2019). Magnetic mineralogy and petrophysical properties of ultramafic rocks: Consequences for crustal magnetism. *Geochemistry, Geophysics, Geosystems*, *20*, 1794–1817. https://doi.org/10.1029/2018GC008132

Weiss, B. P., Vali, H., Baudenbacher, F. J., Kirschvink, J. L., Stewart, S. T., & Shuster, D. L. (2002). Records of an ancient Martian magnetic field in ALH84001. *Earth and Planetary Science Letters*, *201*(3–4), 449–463. https://doi.org/10.1016/S0012-821X(02)00728-8

Xuan, C., & Oda, H. (2019). Sensor response estimate and cross calibration of paleomagnetic measurements on pass-through superconducting rock magnetometers. *Geochemistry, Geophysics, Geosystems*, *20*, 4676–4692. https://doi.org/10.1029/2019GC008597